1 **The role of external inputs and internal cycling in shaping the global ocean cobalt distribution:**
2 **insights from the first cobalt biogeochemical model**
3

4 Alessandro Tagliabue[1*], Nicholas J. Hawco[2,3], Randelle M. Bundy[4,5], William M. Landing[6], Angela
5 Milne[6,7], Peter L. Morton[6,8], and Mak A. Saito[4]
6
7 [1]School of Environmental Sciences, University of Liverpool, Liverpool, United Kingdom
8 [2]MIT-WHOI Joint Program in Oceanography/Applied Ocean Science and Engineering, Department of
9 Marine Chemistry and Geochemistry, Woods Hole Oceanographic Institution, Woods Hole, MA, USA
10 [3]Department of Earth Sciences, University of Southern California, Los Angeles, CA, USA
11 [4]Marine Chemistry and Geochemistry, Woods Hole Oceanographic Institution, Woods Hole, MA
12 [5]School of Oceanography, University of Washington, Seattle, WA, USA
13 [6]Department of Earth, Ocean, and Atmospheric Science, Florida State University, Tallahassee, FL,
14 USA 32306-4320, USA
15 [7]University of Plymouth, Plymouth, PL4 8AA, United Kingdom
16 [8]Geochemistry, National High Magnetic Field Laboratory, Tallahassee, FL, USA
17
18 [*]corresponding author: a.tagliabue@liverpool.ac.uk
19
20 **Abstract**
21

22 Cobalt is an important micronutrient for ocean microbes as it is present in vitamin B_{12} and is a co-
23 factor in various metalloenzymes that catalyse cellular processes. Moreover, when seawater
24 availability of cobalt is compared to biological demands, cobalt emerges as being 'depleted' in
25 seawater, pointing to a potentially important limiting role. To properly account for the potential
26 biological role for cobalt there is therefore a need to understand the processes driving the
27 biogeochemical cycling of cobalt and in particular, the balance between external inputs and internal
28 cycling. To do so, we developed the first cobalt model within a state of the art three-dimensional global
29 ocean biogeochemical model. Overall, our model does a good job in reproducing measurements with
30 a correlation coefficient >0.7 in the surface and >0.5 at depth. We find continental margins are the
31 dominant source of cobalt, with a crucial role played by supply under low bottom-water oxygen
32 conditions. The basin scale distribution of cobalt supplied from margins is facilitated by the activity of
33 manganese oxidising bacteria being suppressed under low oxygen and low temperatures, which
34 extends the residence time of cobalt. Overall, we find a residence time of 7 and 250 years in the upper
35 250m and global ocean, respectively. Importantly, we find that the dominant internal resupply process
36 switches from regeneration and recycling of particulate cobalt to dissolution of scavenged cobalt
37 between the upper ocean and the ocean interior. Our model highlights key regions of the ocean where
38 biological activity may be most sensitive to cobalt availability.
39
40 **1. Introduction**
41
42 When compared to typical phytoplankton requirements, cobalt (Co) emerges as being relatively
43 depleted in seawater [*Moore et al.*, 2013; *Saito et al.*, 2008] and in some ocean regions there is
44 evidence that Co is the primary or secondary limiting nutrient [*Bertrand et al.*, 2015; *Bertrand et al.*,
45 2007; *Browning et al.*, 2017; *Sañudo-Wilhelmy et al.*, 2006]. Marine phytoplankton require Co due to
46 its presence in vitamin B_{12} (also known as cobalamin) and due to its role as a potential co-factor in
47 carbonic anhydrase and alkaline phosphatase, which catalyse carbon fixation and organic phosphorus
48 acquisition, respectively (although a confirmation awaits of a marine pelagic microbe with Co within its
49 alkaline phosphatase [*Wojciechowski et al.*, 2002]). In eukaryotic algae, zinc (Zn) can be substituted
50 for Co in carbonic anhydrase and alkaline phosphatase when Co levels are low [*Morel et al.*, 1994;
51 *Sunda and Huntsman*, 1995], but cyanobacteria are known to have an obligate Co requirement [*Saito*
52 *et al.*, 2002]. Despite the Co-containing vitamin B_{12} playing a fundamental role in the development of

53   the first theories for algal nutrient limitation and its representation in numerical models [*Droop*, 1973;
54   1974], Co cycling remains ignored in contemporary global ocean biogeochemical models.
55
56   While early pioneering studies considered Co to be a 'scavenged-type' element [*Jickells and Burton*,
57   1988], subsequent investigations with lower detection limits identified the nutrient-like depletion in the
58   upper photic zone highlighting the role of biological Co uptake [*Martin et al.*, 1989; *Noble et al.*, 2008;
59   *Saito and Moffett*, 2002]. Thus, Co is better described as a 'hybrid-type' element, with external inputs
60   from continental margins (in particular within the major oxygen minimum zones), as well as riverine,
61   and dust sources [*Noble et al.*, 2012; *Saito and Moffett*, 2002; *Saito et al.*, 2004; *Shelley et al.*, 2012;
62   *Zhang et al.*, 1990]. In addition to these external inputs, Co is strongly removed from the dissolved
63   fraction via scavenging [*Bruland et al.*, 2014; *Moffett and Ho*, 1996]. The scavenging of Co is
64   catalysed by manganese (Mn) oxidizing bacteria, due to the similar ionic radii and redox potentials of
65   Mn and Co [*Cowen and Bruland*, 1985; *Moffett and Ho*, 1996; *Sunda and Huntsman*, 1988].
66
67   Like many bioactive metals, Co is often found strongly bound by natural ligands, particularly in the
68   upper water column [*Michael J Ellwood and van den Berg*, 2001; *Saito and Moffett*, 2001]. These
69   ligands have been shown to be produced from cyanobacteria blooms and released to the ocean upon
70   cell lysis [*Saito et al.*, 2005] and are hypothesized to be important in protecting Co from scavenging
71   and in decreasing Co bioavailability to some phytoplankton when complexed [*Moffett and Ho*, 1996;
72   *Saito et al.*, 2002]. Yet unlike other bioactive metals (e.g. iron), in some regions, Co can also be found
73   to be unsaturated by natural ligands, particularly in coastal and polar regions. This results in
74   measurable concentrations of labile Co that are likely far more bioavailable [*Saito et al.*, 2010; *Saito et*
75   *al.*, 2004]. Thus far, the only known Co ligands are likely to be the cobalamins that are known to be
76   synthesised by some bacteria (including cyanobacteria) and archaea.
77
78   With the arrival of GEOTRACES research cruises at the ocean basin scale, a number of studies have
79   provided detailed data on the distributions of Co in the Atlantic, Pacific and Southern Oceans. The
80   zonal sections identified major plumes of Co in the major oxygen depleted regions of the North and
81   South Atlantic and South Pacific Oceans, extending well into each basin and farther than analogous
82   iron or Mn plumes [*Hawco et al.*, 2016; *Noble et al.*, 2012; *Noble et al.*, 2017], implying lesser Co
83   scavenging. In addition, many of these studies have observed widespread depletions of dCo in the
84   upper ocean, typical of its role as a micronutrient, even in the dust laden North Atlantic Ocean [*Bown*
85   *et al.*, 2011; *Dulaquais et al.*, 2014; *Hawco et al.*, 2016; *Noble et al.*, 2012; *Noble et al.*, 2017]. These
86   large-scale oceanographic Co datasets have facilitated the examination of the links between Co and
87   other parameters, such as positive links with phosphate and nitrous oxide within the euphotic zone,
88   and inverse relationships with dissolved oxygen in the mesopelagic [*Noble et al.*, 2012; *Noble et al.*,
89   2017]. When compared to phosphate, Co is distinguished from other bioactive metals (e.g. cadmium
90   or zinc) in having a wide range of Co:P slopes that span more than an order of magnitude [*Bown et*
91   *al.*, 2011; *Noble et al.*, 2017; *Saito et al.*, 2010; *Saito and Moffett*, 2002], suggestive of variable
92   microbial use. In certain ocean regions, Co section datasets spanned regions known to contain
93   hydrothermal plumes of iron and Mn [*Hatta et al.*, 2015; *Resing et al.*, 2015; *Saito et al.*, 2013], but no
94   corresponding Co plumes were observed [*Hawco et al.*, 2016; *Noble et al.*, 2012; *Noble et al.*, 2017].
95
96   At the global scale, ocean biogeochemical models are excellent platforms with which to explore the
97   differing roles of often competing signals linked to external inputs and internal cycling in different
98   biogeochemical regimes and water masses. In this study, we developed the first representation of Co
99   cycling in a global ocean model and investigated how external inputs and internal cycling shape the
100   oceanic distribution of this important micronutrient. We find key roles played by low oxygen and the
101   suppression of bacterial activity by temperature in promoting the longevity of Co. This then facilitates
102   the widespread impact of Co inputs from the ocean margins at the basin scale.
103
104   **2. Methods**
105

106 We have devised the first global Co model that is coupled to the PISCES-v2 model, which is itself
107 coupled to offline circulation fields within the NEMO framework (www.nemo-ocean.eu). The PISCES-
108 v2 model simulates a wide range of tracers: nitrate, ammonium, phosphate, silicic acid, iron, iron-
109 binding ligands, dissolved oxygen, two size classes of particles, two phytoplankton functional types
110 (diatoms and nanophytoplankton), two grazers, dissolved organic carbon, dissolved inorganic carbon,
111 biogenic silica, calcium carbonate and alkalinity [*Aumont et al.*, 2015; *Tagliabue and Resing*, 2016]. In
112 this work, we have augmented PISCES-v2 with an additional six tracers to resolve the biogeochemical
113 cycling of Co. The additional tracers are: *dCo*: Dissolved cobalt, *scCo*: scavenged cobalt (putatively
114 associated with Mn oxides), $PhyCo_D$: cobalt within diatoms, $PhyCo_N$: cobalt within nanophytoplankton,
115 PCo_S: small particulate organic cobalt and PCo_B: large particulate organic cobalt. The Co within micro
116 zooplankton and mesozooplankton is an inferred quantity driven by a fixed Co/P ratio within
117 zooplankton, which then drives excretion of Co when prey Co is greater than the required Co, as for
118 Fe in PISCES-v2 [*Aumont et al.*, 2015]. All parameter values for the Co model are described in Table
119 1.
120
121 **2.1 Generalised source-sink equations for Co tracers**
122
123 $$d(dCo)/dt = Dust_{Co} + Sed_{Co} + river_{Co} - Up_{Co} - Scav_{Co} + Dissol_{Co} + Excret_{Co} + Remin_{Co} \quad (1)$$
124
125 dCo is supplied from dust ($Dust_{Co}$), sediments (Sed_{Co}) and rivers ($River_{Co}$), with no source from
126 hydrothermal venting based on results from GEOTRACES sections. dCo is consumed by
127 phytoplankton (Up_{Co}) and lost due to scavenging ($Scav_{Co}$). dCo is also resupplied from the dissolution
128 of scCo ($Dissol_{Co}$) and excretion by zooplankton ($Excret_{Co}$) and the remineralisaton of particulate
129 organic cobalt ($Remin_{Co}$).
130
131 $$d(scCo)/dt = Scav_{Co} - Dissol_{Co} - sinking \quad (2)$$
132
133 scCo is produced due to the scavenging of dCo ($Scav_{Co}$) and scCo dissolves via dissolution back to
134 dCo ($Dissol_{Co}$). scCo sinks at 1 m d^{-1}.
135
136 $$d(phyCo_i)/dt = Up_{Coi} - Dissol_{Co} - SMS_i \quad (3)$$
137
138 Phytoplankton Co of functional group *i* (D = diatom, N = nanophytoplankton) is a result of dCo uptake
139 (Up_{Co}), which is explicitly modelled and specific to diatoms and nanophytoplankton (Up_{CoD} and Up_{CoN},
140 respectively, Up_{Co} in Eqn 1 is the sum of both terms). Loss of phytoplankton Co follows the processes
141 of mortality, aggregation and grazing (SMS_i) in the main PISCES-v2 model [*Aumont et al.*, 2015].
142
143
144 $$d(PCo_i)/dt = SMS_i - Remin_{Co} \quad (4)$$
145
146 Remineralisation of Co from small and large organic Co particles (subscript i=S or B, $Remin_{CoS}$ and
147 $Remin_{CoB}$, respectively, $Remin_{Co}$ is the sum of both terms) is modelled independently via a tunable
148 parameter relative to the remineralisation of organic carbon (ϕ). By default, we assume particulate
149 organic Co remineralises 50% faster than organic carbon (ϕ=1.5). Other gains and loss of particulate
150 Co (SMS_S and SMS_B) follow the processes of aggregation, disaggregation, phytoplankton and
151 zooplankton mortality, sinking and grazing as per the main PISCES model [*Aumont et al.*, 2015].
152
153 **2.2 External inputs of Co**
154

155 Dust input assumes a mineral fraction of Co of 17.3 μg g^{-1} [*Rudnick and Gao*, 2014] and a Co
156 solubility of 8% [*Shelley et al.*, 2012] . River supply assumes a Co/C ratio of 12 μmol mol^{-1} [*Gaillardet*
157 *et al.*, 2003]. Sediment Co input (sed$_{Co}$) is modelled via a set of bottom water oxygen (O$_{2bw}$) dependent
158 thresholds and is benchmarked to the sedimentary iron (Fe) supply (sed$_{Fe}$) in the model, which is a
159 function of organic carbon flux to the sediment:

161 O$_{2bw}$ ≤ O$_{2thres\_1}$, sed$_{Co}$ = sed$_{Fe}$ * M * 1000
162 O$_{2bw}$ ≤ O$_{2thres\_2}$, sed$_{Co}$ = 0
163 O$_{2bw}$ > O$_{2thres\_1}$, sed$_{Co}$ = sed$_{Fe}$ * M * 25

165 Where 'M' represent the Co/Fe mineral fraction ratio [*Rudnick and Gao*, 2014]. The 1000 and 25
166 factors are tuned to account for suboxic Co release from dissolution of Fe and Mn oxides under
167 suboxic conditions and Co incorporation into Fe-sulfides (pyrite) under very low O$_2$ when sulphate
168 reduction initiates in porewaters of surface sediments. Specifically, O$_{2thres\_1}$ = 50 μM O$_2$ and O$_{2thres\_2}$ =
169 2 μM O$_2$.

171 In oxic sediments, Co in porewaters is very low <2.5 nM (Heggie and Lewis, 1984), due to rapid Mn
172 oxidation in near-surface sediments where O$_2$ from the water column can penetrate. Oxidation of Co in
173 microbially-catalysed Mn oxidation [*Lee and Fisher*, 1993; *Moffett and Ho*, 1996] limits the diffusive
174 flux out of sediments substantially. Co/Al ratios in continental margin sediments (e.g. South China Sea
175 [*Hu et al.*, 2012; *Hu et al.*, 2013]) reflects crustal Co/Al ratios, likely because most of the Co released
176 by dissolution / weathering / desorption of crustal materials is returned to the sediments via Mn-
177 oxidation in estuaries and coastal seas (i.e. is scavenged [*Hawco et al.*, 2016; *Moffett and Ho*, 1996]).

179 The small flux when O$_2$ > O$_{2\_thres\_1}$ reflects release by sediment desorption, and/or ligand stabilization
180 of Co in estuaries [*Bewers and Yeats*, 1977; *Kharkar et al.*, 1968; *Zhang et al.*, 1990]. Suboxic release
181 of Co has been shown explicitly [*Sundby et al.*, 1986][*Johnson et al.*, 1988], and is reflected in low
182 Co/Al ratios in margin sediments in OMZs off Peru [*Böning et al.*, 2004], Chile [*Böning et al.*, 2009],
183 the Gulf of California [*Brumsack*, 1989] and in the South Atlantic under the Benguela upwelling region
184 [*Bremner and Willis*, 1993]. Co fixation into pyrite formation follows thermodynamic predictions (e.g.
185 [*Morse and Luther*, 1999; *Saito et al.*, 2003]) and can be seen from high Co/Al ratios in Black Sea
186 sediments [*Brumsack*, 2006] and in sulphide-rich sediments near Walvis Bay on the Namibian Coast
187 [*Borchers et al.*, 2005] . The precise choice of the threshold concentrations chosen here reflects model
188 tuning to the dissolved oxygen concentrations in the model, balancing model performance in the
189 Atlantic, Pacific and Indian Oceans.

191 **2.3 Internal cycling of Co**

193 **2.3.1 Phytoplankton uptake**

195 Phytoplankton uptake of Co is explicitly modelled rather than using a 'Redfield' conversion based on
196 the modelled carbon fixation rate. Equation 5 represents this in a similar manner to how PISCES
197 models Fe uptake, accounting for a maximum cellular quota and the potential for uptake to be
198 upregulated under certain conditions [*Aumont et al.*, 2015]. This decouples Co uptake from C fixation
199 and permits variable Co/C ratios as observed [*Sunda and Huntsman*, 1995].

201 $$Up_{Coi} = \mu_{MAXi}\theta_{MAXi} \left. bCo \middle/ (bCo + kbCoi) \right. \frac{(1 - \theta i / \theta_{MAXi})}{(1.05 - \theta i / \theta_{MAXi})} \xi_{Zn} \quad (5)$$

203 Where, subscript i denotes either D (diatoms) or N (nanophytoplankton), bCo is the bioavailable Co
204 pool and is assumed to represent dCo for nanophytoplankton (based on observations/assumptions
205 that cyanobacteria utilize both CoL complexes and Co' [*Saito et al.,* 2002]) and inorganic cobalt

species, Co', for diatoms (based on observations by *Sunda and Huntsman* [1995]; see below for the calculation of Co'), and μ_{MAXi} is the maximum growth rate of functional type i. The Co/P ratio is represented by θ_i within the functional group i and θ_{MAXi} is the maximum Co/P ratio for phytoplankton functional group i, while kbCoi is the half saturation constant for bCo uptake for functional group i. Co uptake is downregulated when θ approaches θ_{MAX} using a hyperbolic function with a shape factor set to 0.5 (as for Fe in PISCES-v2). The term ξ_{Zn} is a scalar active only for diatoms, and represents the inter-replacement of Co and Zn within carbonic anhydrase causing Zn concentrations to affect Co uptake [*Price and Morel*, 1990; *Saito and Goepfert*, 2008; *Sunda and Huntsman*, 1995; *Xu et al.*, 2007] via:

$$\xi_{Zn} = MAX[0.1 , 3 * \left(1 - \frac{Zn}{(Zn + kZnCo)}\right)] \qquad (6)$$

Where kZnCo represents the half saturation constant for Zn-Co interactions. This is initially set to 0.5 nM Zn, which would approximately reflect a free Zn concentration of 5 pM. Previous work has shown enhanced Co uptake when Zn falls below 5-10 pM in several species of eukaryotic phytoplankton [*Sunda and Huntsman*, 1995]. In the absence of a specific Zn model, the Zn concentration (in nM) is derived from Si (in μM) using 0.065 * Si + 0.183 (Lohan pers comm.) as there is a long noted relationship between Zn and Si [*Bruland et al.*, 1978]. The constants 0.1 and 1.3 in Eqn 6, decrease Co uptake by up to 90% when Zn is abundant and increase Co uptake up to 3-fold when Zn is scarce, respectively.

2.3.2 Scavenging and dissolution

The scavenging of dCo is assumed to be driven by Mn oxides produced by Mn oxidising bacteria [*Johnson et al.*, 1988; *Moffett and Ho*, 1996]. At this stage, our model does not include an explicit Mn module so we assume Mn oxides to be prevalent where oxygen is abundant [*Ohnemus and Lam*, 2015; *Ohnemus et al.*, 2017], and that the activity of heterotrophic Mn-oxidising bacteria scales with total bacterial activity [*Cowen and Bruland*, 1985; *Moffett and Ho*, 1996; *Sunda and Huntsman*, 1988]), except in the surface ocean where manganese oxides are destroyed via photo-reduction and dissolution [*Sunda and Huntsman*, 1988]. Co loss is generally controlled by biological uptake in oligotrophic regions [*Moffett and Ho*, 1996]. Although the factors controlling Mn-oxidation remain poorly understood [*Lee and Fisher*, 1993], Mn-oxidation is the likely vector for Co scavenging given, 1) the known ability for Co to be co-oxidized by Mn-oxidizing bacteria [*Lee and Fisher*, 1993; *Moffett and Ho*, 1996], 2) similar redox potentials and ionic radii of Co and Mn [*Moffett and Ho*, 1996; *Swanner et al.*, 2014], 3) extensive covariation between Co and Mn contents of solid-phase marine sediments, manganese nodules, and ferromanganese crusts [*Krishnaswami*, 1976; *Manheim*, 1986], which accumulate Co scavenged from the water column and 4) co-variation of particulate Co and Mn phases in the mesopelagic [*Saito et al.*, 2016]. In addition to oxygen-related cycling of Mn-oxides in sediments, the absence of particulate Mn has been long noted in offshore oxygen minimum zones of the North and South Pacific [*Johnson et al.*, 1996; *Landing and Bruland*, 1987; *Ohnemus et al.*, 2017] and attributed to slow Mn-oxide formation at low O_2 and in situ reduction.

The specific rate of scavenging (Λ) is based on a minimum (ΛCo_{min}) and maximum scavenging rate (ΛCo) that is modulated by oxygen, bacterial activity (itself affected by nutrient and dissolved organic matter limitation) and light:

$$\Lambda = \Lambda_{MIN} + \Lambda Co * Q * kO_2 * kBACT * (1 - kPAR) \qquad (7)$$

Q is the specific temperature function for Co oxidation by manganese oxidising bacteria with a Q_{10} of 2.75 [*Lee and Fisher*, 1993]. The various other terms relate to the impact of oxygen, bacterial activity and light on Co scavenging:

258 $$kO_2 = {(O_2 - O_{2ST})^2} \Big/ {((O_2 - O_{2ST})^2 + kO_2\Lambda^2)} \qquad (8)$$

259
260 Where O_2 is dissolved oxygen, O_{2ST} is the threshold concentration for scavenging and $kO_2\Lambda$ is the half
261 saturation constant for the influence of O_2 on Co scavenging.
262
263 $$kBACT = {BACT^2} \Big/ {(BACT^2 + kB\Lambda^2)} \qquad (9)$$

264
265 BACT is the biomass of bacteria (μM C, see *Aumont et al.* [2015]) and $kB\Lambda$ is the half saturation
266 constant for the influence of bacterial activity on Co scavenging,
267
268 $$kPAR = {PAR^2} \Big/ {(PAR^2 + kPAR\Lambda^2)} \qquad (10)$$

269
270 Where PAR is photosynthetically active radiation, and $kPAR\Lambda$ is the half saturation constant for the
271 influence of irradiance on Co scavenging. The overall loss of dCo (*Scav_Co*) is then governed by the
272 scavenging rate (Λ) and the Co prime concentration (Co') such that *Scav_Co* = $\Lambda*$Co'.
273
274 Since Co-binding ligands are very strong, with $logK_{cond}$ > 16 [*Michael J Ellwood and van den Berg*,
275 2001; *Saito and Moffett*, 2001; *Saito et al.*, 2005] and are found at concentrations that are less than or
276 equal to the dissolved Co concentration, we determine the Co prime (Co') concentration via: Co'=
277 dCo-CoL, where Co' is defined as the sum of inorganic cobalt complexes and Co^{2+}. It should be noted
278 that if there are any weaker organic Co complexes below the detection window of voltammetic studies,
279 then they are part of the labile Co reservoir, which is a measured Co parameter that is often compared
280 with Co'. The oxidation state of Co is not explicitly calculated within the model; however, empirical
281 detection window studies have found that CoL complexes must be in the Co(III) state and solubility
282 estimates require that Co' is Co(II) [*Saito et al.,* 2005].
283
284 Co ligands have been observed to be produced by communities dominated by picocyanobacteria
285 [*Saito et al.*, 2005], and could be sourced from release of intracellular cobalamin/pseudocobalamin
286 cofactors, or their precursors and photodegradation products, during the grazing or viral lysis of
287 microbes in euphotic zone as part of the microbial loop. All sequenced marine cyanobacteria have the
288 genes required for the *de novo* biosynthesis of pseudocobalamin, starting from inorganic Co species
289 [*Helliwell et al.*, 2016]. We therefore link the production of Co ligands to the relative abundance and
290 biomass of nanophytoplankton in our model, although future efforts could consider additional
291 prokaryotic sources. Co ligands have an imposed minimum concentration (CoL_{MIN}) to stabilise dCo in
292 the deep ocean. At present, this component of the model is a simple means to represent Co
293 speciation and does not permit any excess Co binding ligands, although their presence remains
294 debated [*Michael J. Ellwood et al.*, 2005; *Saito and Moffett*, 2001; *Saito et al.*, 2005]. The loss of dCo
295 via scavenging is then: Co' * Λ. At Co' concentrations greater than 100pM, Co' is lost at an elevated
296 rate (10*ΛCo).
297
298 Dissolution of scCo occurs where light is high or O_2 is low:
299
300 $$\lambda = \lambda_{MAX} * MAX[kPAR, kO_2d] \qquad (11)$$

301
302 where kPAR is as per Eqn 10 and
303
304 $$kO_2d = {(O_2 - O_{2DT})^2} \Big/ {((O_2 - O_{2DT})^2 + kO_2\Lambda^2)} \qquad (12)$$

305

306 where O_{2DT} is the threshold concentration for dissolution and λ_{MAX} is the specific rate of scCo
307 dissolution. The specific rate of scCo dissolution is then multiplied by scCo to result in *Dissol_Co*.
308
309 **2.3.4 Excretion and remineralisation**
310
311 Zooplankton excretion of Co is modelled in the same manner as for Fe in PISCES-v2 and is
312 accordingly enhanced when prey are rich in Co, relative to the imposed zooplankton Co quota (Table
313 1). The remineralisation of organic Co, relative to organic P, can be up or down regulated by the scalar
314 ϕ. During model tuning, a 50% faster remineralization rate for Co, relative to P was found to improve
315 the Atlantic – Pacific contrast.
316
317 **2.4 Model experiments and datasets**
318
319 The standard Co model (CTL) was spun up for 1000 years and a range of different experiments were
320 then conducted for 125 years each. To determine the role of specific source processes, we ran
321 experiments with no dust supply (NODUST) and no sediment supply (NOSED). In addition, the effect
322 of oxygen thresholds on coastal sources and scavenging was investigated. We ran experiments where
323 low oxygen did not enhance sediment Co fluxes (NOSEDOX) (i.e. where $O_{2thres\_1} = 0$), and where low
324 oxygen did not switch off sedimentary Co fluxes (NOSEDOXA; i.e. where $O_{2thres\_2} = 0$). We then ran a
325 set of experiments where oxygen did not affect scavenging rates (SCAV1) and where bacterial activity
326 did not affect scavenging rates (SCAV2).
327
328 To assess our Co model, we compiled 8,235 Co data points from a variety of studies. They are
329 compared graphically with the model results as raw data. For the statistical comparisons, the Co
330 observations are gridded on to a 1° x 1° horizontal grid with 33 vertical levels (bounded by 0, 10, 20,
331 30, 40, 50, 75, 100, 125, 150, 200, 250, 300, 400, 500, 600, 700, 800, 900, 1000, 1100, 1200, 1300,
332 1400, 1500, 1750, 2000, 2500, 3000, 3500, 4000, 4500, 5000 and 5500m) to compare directly with the
333 model results on the same grid. We pay particular attention to examining the distributions of dCo along
334 key GEOTRACES and CLIVAR transects in the Atlantic, Pacific and Indian Oceans to evaluate model
335 performance.
336
337 Data from the GEOTRACES GA03, CoFeMUG (GAc01), and GP16 sections are measured by
338 cathodic stripping voltammetry following UV oxidation to destroy organic Co ligands. An analytical
339 ligand, dimethyl glyoxime, binds to cobalt and is reduced with Co at a defined potential of -1.15V,
340 resulting in a reduction peak proportional to the Co concentration. Sample-specific instrument
341 sensitivity is determined with 4 successive 25 pM standard additions and a blank is subtracted. SAFe
342 and GEOTRACES community standards are measured to ensure comparability with other methods.
343
344 Dissolved Co concentrations in samples from CLIVAR lines I8/I9, P16, and I5 were measured using
345 flow-through solid phase extraction systems at FSU/NHMFL [*Milne et al.*, 2010]. For all cruises,
346 samples were UV oxidized for 1.5 hours to destroy organic Co ligands and permit total extraction of
347 Co by the chelating resin (Toyopearl AF-Chelate-650M for P16, Nobias Chelate PA-1 for I8/I9 and I5).
348 Sample aliquots (10-20 mL, 0.024 M HCl) were buffered to pH ~6 with ammonium acetate and flowed
349 through a resin column at 2 mL/min. The captured Co was eluted from the resin using 0.5-1 mL of 1.0
350 M HNO_3 (UHP) and analyzed using HR-ICP-MS (Thermo ELEMENT 2, NHMFL/FSU). Concentrations
351 were quantified using standard additions, blank corrected using aliquots of similarly extracted UHP
352 water (18.2 MOhm-cm), and verified through SAFe (S1 and D2) and GEOTRACES (GS and GD)
353 community standards.
354
355 **3. Results and Discussion**
356
357 **3.1 Modelled Co distribution**
358

359 We have compiled 8,235 dCo observations from the major ocean basins to serve as a basis for
360 evaluating the skill of the base model. In general, the data displays the known 'hybrid' character of
361 dCo in the ocean (Figure 1). The surface ocean dCo levels are low on average, but show high
362 variability, while in the ocean interior dCo increases from the surface to intermediate depth, but then
363 declines from the intermediate to deep ocean (Figure 1). The mean model dCo profile extracted at the
364 same location as the observations does a good job in reproducing the observed behaviour, exhibiting
365 a parallel decline in mean dCo towards the surface ocean and the ocean interior from intermediate
366 water depth (~1000m), with a broadly similar pattern shown by the overall modelled mean dCo (Figure
367 1).
368
369 Spatially, the model is able to capture the major trends in dCo between different ocean regions and as
370 a function of depth (Figure 2). As seen in observations, the Arctic Ocean is particularly dCo rich and
371 declines with depth, whereas elsewhere dCo accumulates with depth, particularly so in the low oxygen
372 regions of the tropical Atlantic, Pacific and Indian Oceans. The major mismatch between the model
373 and observations emerges in the Atlantic Ocean between 700-800m and 900-1000m, where the
374 model underestimates the dCo levels within the low oxygen regions of the Mauritanian and Benguela
375 upwelling areas. The CTL model has a correlation coefficient > 0.7 in the upper 200m and > 0.5 at
376 depths greater than 900m. The Atlantic mismatch between 700-800m drives a correlation coefficient of
377 0.264 in this depth stratum (Table 3). Overall, the model has a correlation coefficient of 0.593 over the
378 entire dataset, which is comparable to the most skillful of global Fe models [*Tagliabue et al.*, 2016].
379
380 Examining three GEOTRACES and three CLIVAR ocean sections reveals the strengths and
381 weaknesses of the CTL model. On the GA-03 transect between Woods Hole and Cape Verde in the
382 North Atlantic subtropical gyre [*Noble et al.*, 2017], the model is able to represent a dCo maxima
383 associated with the eastern and western margins, but these are too muted relative to the data (Figure
384 3a). This is likely driven by dCo removal rates that are too high, too little dCo supply from ocean
385 margins, or an underestimation of regeneration of Co from sinking organic matter [*Noble et al.*, 2017].
386 A similar result is found for the CoFeMUG section across the south subtropical Atlantic [*Noble et al.*,
387 2012] where the margin enhanced dCo is produced by the model, but remains less widespread than
388 the data (Figure 3b). In the Pacific Ocean, the model does an excellent job of reproducing the large
389 dCo plume observed on the GP-16 transect [*Hawco et al.*, 2016] and the low dCo upper ocean values
390 (Figure 3c). The strong dCo maxima observed in the northern part of the Indian Ocean is well
391 reproduced by the model along the CLIVAR I8 and I9 section (Figure 3d). The CLIVAR P16 section
392 provides a unique window into the meridional distribution of dCo throughout the entire Pacific Ocean
393 and our model does a good job in reflecting the low dCo values in the surface ocean and gradual
394 accumulation from south to north (Figure 3e). Finally, the zonal CLIVAR I05 section along the
395 boundary between the Indian and Southern Oceans highlights the low dCo concentrations emanating
396 from the dCo poor Southern Ocean.
397
398 The skill of the model in the Atlantic Ocean is related to the underlying biogeochemical model rather
399 than the Co sub model. Initial tests aimed at examining whether Atlantic dCo could be enhanced by
400 lowering scavenging rates (ΛCo) or enhancing sedimentary dCo fluxes, led to unrealistic
401 accumulations of dCo in the Pacific and Indian basins. These initial tests led us to examine whether
402 the biogeochemical model was over estimating oxygen levels in the Atlantic low oxygen regions, which
403 then led to elevated scavenging rates (via the oxygen dependence of Eqn 7). This was quantified by
404 running an additional experiment where model oxygen is annually restored to World Ocean Atlas
405 climatological values. In this run we observe a marked improvement in the modelled dCo along the
406 GA-03 and CoFeMUG transects (Figure 4). Moreover, the model skill in the 700-800m depth stratum
407 is enhanced two-fold (Table 3). This further emphasises the importance of oxygen in shaping dCo
408 cycling in the ocean interior. There is relatively little change in the modelled dCo sections along the
409 GP-16 and CLIVAR I8 and I9 and P16 sections as the model already represents the low oxygen
410 conditions well in these regions.
411

Our model also produces horizontal and vertical variations in the speciation of dCo. The greatest amounts of Co' (defined as the sum of inorganic Co complexes species and Co^{2+}) in both absolute and relative terms are found in the Arctic surface and interior waters and linked to the interior ocean oxygen minima of the tropical Atlantic, Pacific and Indian oceans (Figure 5). These Co' distributions are consistent with some high latitude observations [*Saito et al.,* 2010] and is in some part controlled by Co organic complexes being linked to the prevalence of nanophytoplankton in the model (based on cyanobacterial evidence, *Saito et al.* 2002), which are less prevalent at high latitudes. Scavenging removal is the other component driving the accumulation of Co'. In our model, Co' is removed by Mn-oxidizing bacteria and it is only where this process is impeded that Co' can accumulate. In the oxygen minima, it is the low levels of oxygen that are restricting scavenging by Mn oxidising bacteria, while in the Arctic Ocean and to some extent the Southern Ocean, it is instead the cold temperatures that lessen the scavenging of Co' via lower bacterial metabolic rates. The ratio of Co' to dCo in the model is often greater than 0.5 in the high dCo plumes in the ocean interior, which is a slight overestimate relative to the available data [*Bown et al.*, 2012; *Hawco et al.*, 2016; *Noble et al.*, 2012].

3.2 Role of external sources

Our sensitivity experiments permit an evaluation as to the role of different Co source processes in different geographic regions. Unsurprisingly, dust supply of Co is most important in the regions of the ocean typified by significant dust deposition from the Sahara, Namibian and Arabian deserts. Nevertheless, the largest effects, found for the tropical Atlantic rarely exceed 5 pmol/L in the upper 50m (Figure 6a) and eliminating the dust Co source (NODUST) does not greatly change the upper 50m dCo from the CTL model (Figure 6b compared with Figure 2a). Dust Co is assumed to have a solubility of 8% [*Shelley et al.*, 2012], so the muted influence of dust Co is mostly due to the low mineral fraction of Co in dust (17.3 μg g^{-1} [*Rudnick and Gao*, 2014]). These model results are consistent with observations and calculations showing small to non-detectable surface dust deposition effects in the Atlantic Ocean [*Noble et al.*, 2012; *Noble et al.*, 2017; *Saito and Moffett*, 2002; *Shelley et al.*, 2012; *Shelley et al.*, 2016].

In contrast to dust, sediments are the major external driver of dCo distributions at the surface and in the ocean interior, with absolute dCo concentrations modified by over 50 pM (Figure 6c and d). Indeed, in this experiment surface Co drops to very low levels <10 pM when sediment Co supply is eliminated (NOSED, Figure 6e). In our model, there are two major components to sediment supply; one is the base sediment Co flux and the second is the enhancement of Co fluxes at low oxygen levels. When the enhanced Co fluxes at low oxygen are removed (NOSEDOX) we can highlight regions where Co supply from sediments is mostly driven by this particular process (Figure 6f and g) and the ensuing influence on surface dCo (Figure 6h). By then comparing the results of NOSED with NOSEDOX we can calculate the percentage influence of low oxygen sediment fluxes on dCo. This calculation shows that in the tropical ocean, over half of the influence of sediment Co supply is governed by low oxygen enhancing fluxes, whereas in the Arctic ocean, the strong sensitivity to sediment Co fluxes is driven by the large shelf areas (Figure 6i and j).

Our model does not include hydrothermal input of dCo. While this could be included in the model in a similar manner as for Fe [*Tagliabue and Resing*, 2016], there is no evidence for large basin scale dCo plumes alongside notable hydrothermal Fe signals [*Hawco et al.*, 2016; *Noble et al.*, 2012], despite observations of near-field localized sources [*Noble et al.,* 2017 and references therein].

3.3 Role of internal cycling

We also conducted a set of sensitivity experiments examining the role of various removal processes affecting dCo in the ocean interior. In all these experiments, the Co loss due to a specific process was removed, allowing us to examine how a given process contributes to maintaining the modelled dCo levels.

To firstly consider oxygen, Figure 7a and b show the impact of eliminating the reduction in scavenging by low O_2 levels (Eqn 8) at the surface and 250m. In this experiment, scavenging rates are higher and a clear effect in the tropical ocean emerges where low subsurface O_2 levels contribute upwards of 50pM to the dCo signal (Figure 7b). In regions where low O_2 zones in the ocean interior are coupled to the surface by upwelling, decreased Co scavenging at low O_2 increases surface ocean dCo by up to 10-20pM (Figure 7a). In the oxygen rich high latitude oceans, there is little effect of low O_2 on lessening Co scavenging.

Eliminating the reduction in Co scavenging due to low levels of Mn-oxidizing bacterial activity (Eqn 9) has a different pattern to O_2 (Figure 7 c and d). This parameterization for temperature-based controls on scavenging was based on laboratory experiments with Mn-oxidizing bacteria [*Lee and Fisher*, 1993] and field observations for limited dCo scavenging in the Ross Sea and under the sea-ice [*Saito et al,* 2010; *Noble et al.,* 2013]. The Arctic Ocean now emerges as the strongest signal, both at depth and at the surface (dCo declines by more than 80pM when variations in bacterial rates are ignored). When linked to the strong role for sediment Co supply in this region (section 3.2), this indicates that the low rates of bacterial activity in these cold waters permits sedimentary Co to have a greater influence on dCo levels. The low latitude ocean is also impacted by the greater rates of Co scavenging when low levels of bacterial activity are eliminated. The impact of bacteria is broadly similar to O_2, but much more widespread, both at the surface and at depth.

3.4 The southern equatorial Pacific Co plume: A case study

The GEOTRACES GP16 cruise to the southern equatorial Pacific observed a notable offshore dCo plume in the subsurface ocean emanating from the Peru margin [*Hawco et al.*, 2016]. Our new Co model provides a way in which to assess how external input and internal cycling processes govern this high Co feature. As seen previously, the model is able to reproduce the intensity and magnitude of the observed plume (Figure 8a and b) better than the low oxygen associated Atlantic plumes (see above). We use our suite of sensitivity tests to quantify by how much the dCo plume declines when sedimentary Co supply and the decreased scavenging of Co driven by low O_2 and low rates of bacterial activity are removed. More than 70% of the dCo signal is eliminated by removing sedimentary Co supply very close to the margin, with the impact lessening further offshore (Figure 8c). The low O_2 enhancement of sedimentary Co fluxes supports ~25% of the dCo plume (Figure 8d). The impact of low rates of scavenging due to the low O_2 levels are muted very close to the margin, but become much more important offshore (Figure 8e). This pattern is more marked for the role of low bacterial activity enhancing dCo levels, with little impact close to the margin but a greater impact offshore (Figure 8e). Thus, our model suggests that this dCo plume is initially controlled by high rates of sedimentary Co input close to the margin, but that Co is then maintained in the dissolved pool by low rates of scavenging, firstly due to low O_2 and then due to low rates of bacterial activity in the ocean interior.

4. A synthesis of the ocean cobalt cycle

We can use our model to bring together the first synthesis of the major external inputs and internal cycling of Co in the global ocean. Figure 9 shows the vertically integrated fluxes of Co due to dust and sediment supply (Figure 9a and b), biogeochemical processes of phytoplankton uptake and regeneration (Figure 9c and d), and the scavenging and dissolution of scavenged Co (Figure 9e and f). What becomes apparent is the strong influence of sediment fluxes at ocean boundaries that must then be transported widely by low interior scavenging rates. In our model, almost two-thirds of the total global sedimentary boundary flux of Co is driven by our parametrisation of enhanced supply when low bottom water oxygen is low. This points to a need for further studies on how bottom water oxygen levels modulate Co sediment supply. Co loss due to phytoplankton uptake and resupply due to regeneration are unsurprisingly associated with typical patterns of ocean biological productivity (Figure

518 9c and d). In a similar manner to the spatial coupling between Co consumption by biology and
519 regeneration, Co scavenging and dissolution are spatially linked (Figure 9e and f). It is notable that low
520 O_2 regions dissolve scavenged Co to dCo because of enhanced rates of scCo dissolution. This is not
521 apparent in the higher O_2 regions of the high latitudes. In these regions, e.g. the Arctic, our model
522 predicts that low temperatures decrease the activity of Mn-oxidising bacteria yielding a lower
523 scavenging removal of dCo.
524
525 Our model is able to provide the first estimates of the major global fluxes shaping the oceanic cycle of
526 Co and the ocean residence time of Co (Figure 10). Dust, sediments and rivers supply $6.5x10^7$,
527 $6.8x10^8$ and $5.7x10^6$ moles of Co annually. The sediment source compares favourably to an
528 independent estimate (~$6x10^8$ moles of Co annually) based on simpler calculations from field datasets
529 [*Hawco et al.*, 2017]. Primary Production consumes $23.9x10^8$ moles of Co, with much of this dCo sink
530 balanced by recycling of $20.9x10^8$ moles from zooplankton, while regeneration of particulate organic
531 Co resupplies a further $8.6x10^8$ moles each year. Globally, $3.1x10^8$ and $2.5x10^8$ moles of particulate
532 Co (including organic and scavenged Co particles) sink across the 100m and 250m depth horizons
533 each year, respectively. Scavenging removes $6.8x10^8$ moles from the dCo pool and dissolution of
534 scavenged Co returns moles $4.0x10^8$ per year. When combined with the total Co inventory of the
535 ocean in our model ($5x10^{10}$ moles) the total Co inputs of $7.5x10^8$ moles per year result in a global
536 ocean Co residence time of 70 years. If this is split into upper 250m and deeper than 250m, then the
537 residence times (ignoring physical exchanges) are approximately 7 years in the surface ocean and
538 around 250 years deeper than 250m, similar to simpler early estimates [*Bewers and Yeats*, 1977;
539 *Saito and Moffett*, 2002].
540
541 The internal cycling of Co at the global scale is driven by different processes between the surface
542 ocean and the ocean interior. Unsurprisingly, biological uptake and Co turnover by zooplankton are
543 the major Co sink and source terms in the upper 250m ($23.9x10^8$ and $20.7 x10^8$ mol yr^{-1}) where they
544 dominates over the scavenging sink ($3x10^8$ mol yr^{-1}). In addition to zooplankton recycling, resupply of
545 dCo in the upper 250m by particulate organic Co remineralisation ($8.5x10^8$ mol yr^{-1}) is around double
546 that from the dissolution of scavenged Co ($4x10^8$ mol yr^{-1}). Turning next to the ocean interior (>250m),
547 we find that dissolution of scavenged Co driven by low oxygen is the greatest dCo source globally
548 ($3x10^8$ mol yr^{-1}) and is more than four times greater than remineralisation of particulate organic Co
549 ($0.7x10^8$ mol yr^{-1}, with zooplankton recycling reduced to $0.2x10^8$ mol yr^{-1}). This switch in the dominant
550 internal sources with depth is notable and may be unique to cobalt's biogeochemistry, with
551 remineralization and recycling dominating in the upper water column and the dissolution of scavenged
552 Co within the OMZs in the mesopelagic. Our emphasis on biological uptake in the upper 250m agrees
553 with a previous Co budget from the Atlantic Ocean [*Dulaquais et al.*, 2014]. However, in contrast to
554 *Dulaquais et al.* [2014], we find dissolution of scavenged Co (putatively associated with Mn oxides) to
555 be more important than organic Co remineralisation in the ocean interior (deeper than 250m) in our
556 model. This difference likely reflects the fact that the work of *Dulaquais et al.* [2014] occurred in the
557 relatively oxic Atlantic Ocean and dissolution of scCo will be much more important when the low
558 oxygen zones of the Pacific and Indian Oceans are included (as in our global assessment). Our view
559 is also consistent with observations of large dCo plumes within each of these major oxygen minimum
560 zones [*Noble et al.,* 2012; *Hawco et al.,* 2016; *Noble et al.,* 2017]. Equally, it should be noted that
561 particulate organic Co fluxes attenuate exponentially with depth, accounting for their greater
562 importance in the upper 250m and lesser role (in absolute terms) deeper than 250m. Finally, we
563 highlight that these represent gross integrated fluxes from the model and a given Co atom may
564 participate in more than one process during its lifetime in the ocean, e.g. be remineralised from PCo,
565 then scavenged to scCo and then dissolved back to dCo from scCo.
566
567 Our model has provided us with a conceptual view of how Co is transported from boundary sources
568 into the ocean interior. The southern equatorial Pacific case study suggested that a strong source
569 must be coupled with low scavenging rates to facilitate transfer throughout the ocean. The model
570 experiments show that direct Co supply by dust is negligible apart from some very local regions in the

571 tropical Atlantic Ocean. In the equatorial latitudes of the Pacific and also the Atlantic Ocean, low O_2
572 plays a key role in promoting Co transport by decreasing scavenging. This is seen by the imprint of
573 high Co upon the meridional structure of the Atlantic and Pacific phosphate (PO_4) distributions at low
574 latitudes (Figure 11). Additional decoupling between Co and PO_4 is observed at high latitudes in the
575 Atlantic and Pacific. In the North Pacific, the model proposes an accumulation of dCo due to declining
576 O_2 in the oldest waters at intermediate water depth (which has some support in CLIVAR data, Figure
577 3f and other North Pacific datasets (M. Saito pers. comm.)), while in the North Atlantic high Co from
578 the Arctic is transported equatorward (Figure 11). The Arctic is O_2 rich, compared to the low latitudes,
579 and this region acts as a Co hotspot because high rates of Co input from the shallow shelves are
580 coupled with low rates of removal due to cold temperatures depressing bacterial activity. In the
581 Southern Ocean, shelves are narrower than in the Arctic, leading to lower Co input and little impact on
582 dCo levels due to the scavenging loss in this highly oxic region. Ultimately, our model suggests that
583 scavenging-dissolution processes and their modulation by oxygen levels and bacterial activity are the
584 key determinants of the oceanic distribution of Co. Future studies characterizing the chemistry and
585 biology of Co scavenging are warranted, in particular the generation of in situ estimates of kinetic
586 scavenging rates, to better constrain this process.
587
588 **5. Towards quantifying the biological role of cobalt**
589
590 In general, modelled phytoplankton Co quotas are lowest in the productive regions of the ocean and
591 are highest in the oligotrophic gyres (Figure 12 a and b). This reflects the fact that Co uptake in our
592 model is independent of carbon and phosphorus (P) uptake and thus Co uptake can continue when
593 growth rates (and C and P assimilation rates) are low. Due to the influence of Zn on Co uptake in
594 diatoms, Co/P ratios are lowest for diatoms in the Zn-rich Southern Ocean. Over the seasonal cycle
595 nanophytoplankton and diatom Co/P quotas can reach minimum values of ~60 and <10 μmol/mol
596 (Figure 12 c and d) due to seasonal dCo depletion. Consistent with their overall low levels of
597 phytoplankton biomass, absolute quantities of Co present in phytoplankton biomass are minimum in
598 the oligotrophic gyres.
599
600 Modelled Co/P phytoplankton quotas reflect the observations compiled thus far from synchrotron X-
601 Ray fluorescence methods [*Twining and Baines*, 2013; *Twining et al.*, 2011; *Twining et al.*, 2015].
602 These datasets find Co/P quotas in the temperate Pacific Ocean of <50 μmol/mol for diatoms and
603 >150 μmol/mol for non-diatoms [*King et al.*, 2012], while in the Equatorial Pacific Ocean Co/P quotas
604 are <100 μmol/mol for diatoms and >150 μmol/mol for non-diatoms [*Twining et al.*, 2011] and the CTL
605 model is able to reproduce these limited observations (Figure 12 a-d). The model finds that the
606 subtropical north Atlantic Ocean displays elevated Co/P quotas for both diatoms and
607 nanophytoplankton and these are broadly reflected in the elevated cell quotas of 50-170 μmol/mol
608 measured along GA-03 [*Twining et al.*, 2015].
609
610 The Co/P ratio of the bulk particulate pool reflects the combination of the amalgamation of distinct
611 assemblage quotas and any additional production of particulate Co via scavenging, but does not
612 include lithogenic Co. In general, the pattern (Figure 12e) represents that discussed previously for the
613 phytoplankton. Co/P ratios are low (<100 μmol/mol) in regions of high growth rate and in the Southern
614 Ocean where the dominant diatom demand for Co is repressed by elevated Zn levels. In contrast,
615 Co/P ratios are greatest (>150 μmol/mol) in the tropical Atlantic and Indian Oceans. Notably this is
616 without including any Co substitution within alkaline phosphatase of the dominant cyanobacteria
617 populations in the model, which is suggested by observations of this metalloenzyme within regions of
618 'accelerating' dCo:PO_4 stoichiometries [*Saito et al.*, 2016]. Finally, it is noteworthy that the Co/P ratios
619 increase strongly with depth due to the production of additional particulate Co from the interior ocean
620 scavenging of dCo by Mn-oxidizing bacteria (Figure 12f).
621
622 Ultimately, it is important to link the oceanic distributions and phytoplankton Co quotas to biological
623 activity. At present, Co is known to have two major biological roles. Firstly, vitamin B_{12} or cobalamin

624 contains Co and is mainly required for the synthesis of the amino acid methionine and the nucleotide
625 biosynthesis through the enzymes methionine synthase and ribonucleotide reductase, respectively
626 [*Bertrand et al.*, 2013; *Rodionov et al.*, 2003]. Secondly, it is known that Co can act as a substitute co-
627 factor for Zn in carbonic anhydrase [*Morel et al.*, 1994].

629 In our model, we accounted for the impact of Zn on Co requirements via Eqn 6. The precise degree of
630 up or down regulation of phytoplankton Co uptake is largely unknown due to variations in the diversity
631 of Zn/Co cambialism, hence its parameterization is relatively subjective at this stage. Nevertheless,
632 the direction of change across the surface ocean is driven by Zn availability and should be relatively
633 robust. Fig 13 displays the relative change in Co uptake due to Zn (Eqn 6) and shows that maximum
634 impact of Zn on Co requirements should be occurring in the oligotrophic gyres of the Pacific Ocean as
635 Zn is depleted, followed by the southern subtropical Atlantic and the northern subtropical Atlantic
636 gyres. Moreover, Zn-Co interactions may be further exacerbated in oligotrophic systems due to the
637 connection between P scarcity and Zn/Co requirements that could explain high Co:P quotas in the
638 surface Atlantic Ocean [*Saito et al.*, 2016; *Shaked et al.*, 2006]. On the other hand, high levels of Zn in
639 the Southern Ocean should lessen Co demands. Of course, this relies on the fact that we can broadly
640 reconstruct Zn distributions from the close link between Zn and Si. In the future, it would be important
641 to also develop a prognostic ocean Zn model that can be coupled to the current model.

643 At present, models such as PISCES do not account for vitamin regulation of phytoplankton physiology
644 nor impact of Co or Zn scarcity affecting cellular enzymes. Instead such global models tend to rely on
645 identifying the most limiting resource that then governs carbon fixation rates. While some models are
646 moving away from using the external nutrient concentration of resources to drive growth rates
647 [*Arteaga et al.*, 2014; *Aumont et al.*, 2015], they still rely on a limited suite of resources and on 'law of
648 the minimum' parameterisations. In the future, it is important for models to expand their scope beyond
649 N, P, Si and Fe to consider other important resources, such as Co, that are known to be depleted in
650 seawater [*Moore et al.*, 2013] and to revisit the resource limitation parametrizations to account for the
651 potentially important co-limitation between different resources. By way of an example, we found that
652 diatom Co dropped markedly in the NOSED and NOSEDOX highlighting how remote sources from
653 ocean boundaries supports Co nutrition and also implying that changes in boundary sources and their
654 propagation into the ocean interior due to past or future climate change may affect Co limitation.

656 **6. Conclusions**

658 Overall, our model does a good job in reproducing the growing dataset of dCo measurements arising
659 from the GEOTRACES and CLIVAR efforts, and allows for some of the first global-scale estimates of
660 Co fluxes. We find an upper ocean residence time for Co of 7 years, and a deep ocean residence time
661 of 250 years, similar to previous estimates based on smaller datasets [*Bewers and Yeats*, 1977; *Saito*
662 *and Moffett*, 2002]. Our model highlights the sediments as the major external input of Co to the ocean
663 and the importance of reduced scavenging removal in low oxygen regions such as the eastern tropical
664 Pacific, and cold regions such as the Arctic, in propagating Co throughout the ocean. The Arctic and
665 Indian Oceans and low latitude upwelling systems are found to be the most Co rich regions of the
666 ocean, with the Southern Ocean and then the oligotrophic gyres as the most Co poor. Therefore,
667 these Co poor regions may be areas where Co has an impact on biological activity. Representing the
668 impact of Co on microbial vital rates will however, require a greater level of detail in the modelling of
669 phytoplankton physiology in global models to account for resource substitution and co-limitation. Such
670 advances will shed important insights on metal quotas in marine phytoplankton given any future
671 changes to external inputs and internal cycling of micronutrients.

673 **7. Acknowledgements**

8. References:

Arteaga, L., M. Pahlow, and A. Oschlies (2014), Global patterns of phytoplankton nutrient and light
colimitation inferred from an optimality-based model, *Global Biogeochemical Cycles*, *28*(7), 648-661,
doi:10.1002/2013gb004668.

Aumont, O., C. Ethé, A. Tagliabue, L. Bopp, and M. Gehlen (2015), PISCES-v2: an ocean
biogeochemical model for carbon and ecosystem studies, *Geoscientific Model Development*, *8*(8),
2465-2513, doi:10.5194/gmd-8-2465-2015.

Bertrand, E. M., et al. (2015), Phytoplankton-bacterial interactions mediate micronutrient colimitation at
the coastal Antarctic sea ice edge, *Proceedings of the National Academy of Sciences of the United
States of America*, *112*(32), 9938-9943, doi:10.1073/pnas.1501615112.

Bertrand, E. M., D. M. Moran, M. R. McIlvin, J. M. Hoffman, A. E. Allen, and M. A. Saito (2013),
Methionine synthase interreplacement in diatom cultures and communities: Implications for the
persistence of B12use by eukaryotic phytoplankton, *Limnology and Oceanography*, *58*(4), 1431-1450,
doi:10.4319/lo.2013.58.4.1431.

Bertrand, E. M., M. A. Saito, J. M. Rose, C. R. Riesselman, M. C. Lohan, A. E. Noble, P. A. Lee, and
G. R. DiTullio (2007), Vitamin B12and iron colimitation of phytoplankton growth in the Ross Sea,
Limnology and Oceanography, *52*(3), 1079-1093, doi:10.4319/lo.2007.52.3.1079.

Bewers, J., and P. Yeats (1977), Oceanic residence times of trace metals, *Nature*, *268*(5621), 595-
598.

Böning, P., H.-J. Brumsack, M. E. Böttcher, B. Schnetger, C. Kriete, J. Kallmeyer, and S. L. Borchers
(2004), Geochemistry of Peruvian near-surface sediments, *Geochimica et Cosmochimica Acta*, *68*,
4429-4451, doi:10.1016/j.gca.2004.04.027.

Böning, P., H.-J. Brumsack, B. Schnetger, and M. Grunwald (2009), Trace element signatures of
Chilean upwelling sediments at ~36°S, *Marine Geology*, *259*(1-4), 112-121,
doi:10.1016/j.margeo.2009.01.004.

Borchers, S. L., B. Schnetger, P. Böning, and H. J. Brumsack (2005), Geochemical signatures of the
Namibian diatom belt: Perennial upwelling and intermittent anoxia, *Geochemistry, Geophysics,
Geosystems*, *6*(6), doi:10.1029/2004gc000886.

Bown, J., M. Boye, A. Baker, E. Duvieilbourg, F. Lacan, F. Le Moigne, F. Planchon, S. Speich, and D.
M. Nelson (2011), The biogeochemical cycle of dissolved cobalt in the Atlantic and the Southern
Ocean south off the coast of South Africa, *Marine Chemistry*, *126*(1-4), 193-206,
doi:10.1016/j.marchem.2011.03.008.

Bown, J., M. Boye, and D. M. Nelson (2012), New insights on the role of organic speciation in the
biogeochemical cycle of dissolved cobalt in the southeastern Atlantic and the Southern Ocean,
Biogeosciences, *9*(7), 2719-2736, doi:10.5194/bg-9-2719-2012.

721 Bremner, J. M., and J. P. Willis (1993), Mineralogy and geochemistry of the clay fraction of sediments
722 from the Namibian continental margin and the adjacent hinterland, *Marine Geology*, *115*, 85-116,
723 doi:10.1016/0025-3227(93)90076-8.

724 Browning, T. J., E. P. Achterberg, I. Rapp, A. Engel, E. M. Bertrand, A. Tagliabue, and C. M. Moore
725 (2017), Nutrient co-limitation at the boundary of an oceanic gyre, *Nature*, doi:10.1038/nature24063.

726 Bruland, K. W., G. A. Knauer, and J. H. Martin (1978), Zinc in Northeast Pacific Water, *Nature*,
727 *271*(5647), 741-743, doi:10.1038/271741a0.

728 Bruland, K. W., R. Middag, and M. C. Lohan (2014), Controls of Trace Metals in Seawater, *Treatise on*
729 *Geochemistry, 2nd edition*, 19-51, doi:10.1016/b978-0-08-095975-7.00602-1.

730 Brumsack, H.-J. (1989), Geochemistry of recent TOC-rich sediments from the Gulf of California
731 and the Black Sea, *Geologische Rundschau*, *78*, 851-882, doi:10.1007/BF01829327.

732 Brumsack, H.-J. (2006), The trace metal content of recent organic carbon-rich sediments: Implications
733 for Cretaceous black shale formation, *Palaeogeography, Palaeoclimatology, Palaeoecology*, *232*, 344-
734 361, doi:10.1016/j.palaeo.2005.05.011.

735 Cowen, J. P., and K. W. Bruland (1985), Metal deposits associated with bacteria: implications for Fe
736 and Mn marine biogeochemistry, *Deep Sea Research Part A. Oceanographic Research Papers*, *32*,
737 253-272, doi:10.1016/0198-0149(85)90078-0.

738 Droop, M. R. (1973), Some Thoughts on Nutrient Limitation in Algae, *Journal of Phycology*, *9*(3), 264-
739 272, doi:10.1111/j.1529-8817.1973.tb04092.x.

740 Droop, M. R. (1974), The nutrient status of algal cells in continuous culture, *Journal of the Marine*
741 *Biological Association of the United Kingdom*, *54*(04), 825, doi:10.1017/s002531540005760x.

742 Dulaquais, G., M. Boye, R. Middag, S. Owens, V. Puigcorbe, K. Buesseler, P. Masqué, H. J. W. de
743 Baar, and X. Carton (2014), Contrasting biogeochemical cycles of cobalt in the surface western
744 Atlantic Ocean, *Global Biogeochemical Cycles*, *28*(12), 1387-1412, doi:10.1002/2014gb004903.

745 Ellwood, M. J., and C. M. van den Berg (2001), Determination of organic complexation of cobalt in
746 seawater by cathodic stripping voltammetry, *Marine Chemistry*, *75*(1), 33-47.

747 Ellwood, M. J., C. M. G. van den Berg, M. Boye, M. Veldhuis, J. T. M. de Jong, H. J. W. de Baar, P. L.
748 Croot, and G. Kattner (2005), Organic complexation of cobalt across the Antarctic Polar Front in the
749 Southern Ocean, *Marine and Freshwater Research*, *56*(8), 1069-1075,
750 doi:https://doi.org/10.1071/MF05097.

751 Gaillardet, J., J. Viers, and B. Dupré (2003), Trace Elements in River Waters, *Treatise on*
752 *Geochemistry*, 225-272, doi:10.1016/b0-08-043751-6/05165-3.

753 Hatta, M., C. I. Measures, J. Wu, S. Roshan, J. N. Fitzsimmons, P. Sedwick, and P. Morton (2015), An
754 overview of dissolved Fe and Mn distributions during the 2010–2011 U.S. GEOTRACES north Atlantic
755 cruises: GEOTRACES GA03, *Deep Sea Research Part II: Topical Studies in Oceanography*, *116*,
756 117-129, doi:10.1016/j.dsr2.2014.07.005.

757 Hawco, N. J., P. J. Lam, J.-M. Lee, D. C. Ohnemus, A. E. Noble, N. J. Wyatt, M. C. Lohan, and M. A.
758 Saito (2017), Cobalt scavenging in the mesopelagic ocean and its influence on global mass balance:
759 Synthesizing water column and sedimentary fluxes, *Marine Chemistry*,
760 doi:10.1016/j.marchem.2017.09.001.

15

761   Hawco, N. J., D. C. Ohnemus, J. A. Resing, B. S. Twining, and M. A. Saito (2016), A dissolved cobalt
762   plume in the oxygen minimum zone of the eastern tropical South Pacific, *Biogeosciences*, *13*(20),
763   5697.

764   Helliwell, K. E., A. D. Lawrence, A. Holzer, U. J. Kudahl, S. Sasso, B. Krautler, D. J. Scanlan, M. J.
765   Warren, and A. G. Smith (2016), Cyanobacteria and Eukaryotic Algae Use Different Chemical Variants
766   of Vitamin B12, *Curr Biol*, *26*(8), 999-1008, doi:10.1016/j.cub.2016.02.041.

767   Hu, D., P. Böning, C. M. Köhler, S. Hillier, N. Pressling, S. Wan, H. J. Brumsack, and P. D. Clift
768   (2012), Deep sea records of the continental weathering and erosion response to East Asian monsoon
769   intensification since 14ka in the South China Sea, *Chemical Geology*, *326-327*, 1-18,
770   doi:10.1016/j.chemgeo.2012.07.024.

771   Hu, D., P. D. Clift, P. Böning, R. Hannigan, S. Hillier, J. Blusztajn, S. Wan, and D. Q. Fuller (2013),
772   Holocene evolution in weathering and erosion patterns in the Pearl River delta, *Geochemistry,*
773   *Geophysics, Geosystems*, *14*(7), 2349-2368, doi:10.1002/ggge.20166.

774   Jickells, T. D., and J. D. Burton (1988), Cobalt, copper, manganese and nickel in the Sargasso Sea,
775   *Marine Chemistry*, *23*(1-2), 131-144, doi:10.1016/0304-4203(88)90027-8.

776   Johnson, K. S., K. H. Coale, W. M. Berelson, and R. Michael Gordon (1996), On the formation of the
777   manganese maximum in the oxygen minimum, *Geochimica et Cosmochimica Acta*, *60*, 1291-1299,
778   doi:10.1016/0016-7037(96)00005-1.

779   Johnson, K. S., P. M. Stout, W. M. Berelson, and C. M. Sakamoto-Arnold (1988), Cobalt and copper
780   distributions in the waters of Santa Monica Basin, California, *Nature*, *332*, 527-530,
781   doi:10.1038/332527a0.

782   Kharkar, D., K. Turekian, and K. Bertine (1968), Stream supply of dissolved silver, molybdenum,
783   antimony, selenium, chromium, cobalt, rubidium and cesium to the oceans, *Geochimica et*
784   *Cosmochimica Acta*, *32*(3), 285-298.

785   King, A. L., S. A. Sanudo-Wilhelmy, P. W. Boyd, B. S. Twining, S. W. Wilhelm, C. Breene, M. J.
786   Ellwood, and D. A. Hutchins (2012), A comparison of biogenic iron quotas during a diatom spring
787   bloom using multiple approaches, *Biogeosciences*, *9*(2), 667-687, doi:10.5194/bg-9-667-2012.

788   Krishnaswami, S. (1976), Authigenic transition elements in Pacific pelagic clays, *Geochimica et*
789   *Cosmochimica Acta*, *40*, 425-434, doi:10.1016/0016-7037(76)90007-7.

790   Landing, W. M., and K. W. Bruland (1987), The contrasting biogeochemistry of iron and manganese in
791   the Pacific Ocean, *Geochimica et Cosmochimica Acta*, *51*(1), 29-43, doi:10.1016/0016-
792   7037(87)90004-4.

793   Lee, B.-G., and N. S. Fisher (1993), Microbially mediated cobalt oxidation in seawater revealed by
794   radiotracer experiments, *Limnology and Oceanography*, *38*(8), 1593-1602,
795   doi:10.4319/lo.1993.38.8.1593.

796   Manheim, F. T. (1986), Marine cobalt resources, *Science*, *232*(4750), 600-608,
797   doi:10.1126/science.232.4750.600.

798   Martin, J. H., R. M. Gordon, S. Fitzwater, and W. W. Broenkow (1989), Vertex - Phytoplankton Iron
799   Studies in the Gulf of Alaska, *Deep-Sea Res*, *36*(5), 649-&, doi:10.1016/0198-0149(89)90144-1.

800 Milne, A., W. Landing, M. Bizimis, and P. Morton (2010), Determination of Mn, Fe, Co, Ni, Cu, Zn, Cd
801 and Pb in seawater using high resolution magnetic sector inductively coupled mass spectrometry (HR-
802 ICP-MS), *Analytica chimica acta*, *665*(2), 200-207, doi:10.1016/j.aca.2010.03.027.

803 Moffett, J. W., and J. Ho (1996), Oxidation of cobalt and manganese in seawater via a common
804 microbially catalyzed pathway, *Geochimica et Cosmochimica Acta*, *60*, 3415-3424, doi:10.1016/0016-
805 7037(96)00176-7.

806 Moore, C. M., et al. (2013), Processes and patterns of oceanic nutrient limitation, *Nature Geoscience*,
807 doi:10.1038/ngeo1765.

808 Morel, F. M. M., J. R. Reinfelder, S. B. Roberts, C. P. Chamberlain, J. G. Lee, and D. Yee (1994), Zinc
809 and Carbon Co-Limitation of Marine-Phytoplankton, *Nature*, *369*(6483), 740-742, doi:Doi
810 10.1038/369740a0.

811 Morse, J., and G. Luther (1999), Chemical influences on trace metal-sulfide interactions in anoxic
812 sediments, *Geochimica et Cosmochimica Acta*, *63*(19), 3373-3378.

813 Noble, A. E., et al. (2012), Basin-scale inputs of cobalt, iron, and manganese from the Benguela-
814 Angola front to the South Atlantic Ocean, *Limnology and Oceanography*, *57*(4), 989-1010,
815 doi:10.4319/lo.2012.57.4.0989.

816 Noble, A. E., D. C. Ohnemus, N. J. Hawco, P. J. Lam, and M. A. Saito (2017), Coastal sources, sinks
817 and strong organic complexation of dissolved cobalt within the US North Atlantic GEOTRACES
818 transect GA03, *Biogeosciences*, *14*(11), 2715-2739, doi:10.5194/bg-14-2715-2017.

819 Noble, A. E., M. A. Saito, K. Maiti, and C. R. Benitez-Nelson (2008), Cobalt, manganese, and iron
820 near the Hawaiian Islands: A potential concentrating mechanism for cobalt within a cyclonic eddy and
821 implications for the hybrid-type trace metals, *Deep Sea Research Part II: Topical Studies in*
822 *Oceanography*, *55*(10-13), 1473-1490, doi:10.1016/j.dsr2.2008.02.010.

823 Ohnemus, D. C., and P. J. Lam (2015), Cycling of lithogenic marine particles in the US GEOTRACES
824 North Atlantic transect, *Deep Sea Research Part II: Topical Studies in Oceanography*, *116*, 283-302,
825 doi:10.1016/j.dsr2.2014.11.019.

826 Ohnemus, D. C., S. Rauschenberg, G. A. Cutter, J. N. Fitzsimmons, R. M. Sherrell, and B. S. Twining
827 (2017), Elevated trace metal content of prokaryotic communities associated with marine oxygen
828 deficient zones, *Limnology and Oceanography*, *62*(1), 3-25, doi:10.1002/lno.10363.

829 Price, N., and F. Morel (1990), Cadmium and cobalt substitution for zinc in a marine diatom, *Nature*,
830 *344*(6267), 658.

831 Resing, J. A., P. N. Sedwick, C. R. German, W. J. Jenkins, J. W. Moffett, B. M. Sohst, and A.
832 Tagliabue (2015), Basin-scale transport of hydrothermal dissolved metals across the South Pacific
833 Ocean, *Nature*, *523*(7559), 200-203, doi:10.1038/nature14577.

834 Rodionov, D. A., A. G. Vitreschak, A. A. Mironov, and M. S. Gelfand (2003), Comparative genomics of
835 the vitamin B12 metabolism and regulation in prokaryotes, *J Biol Chem*, *278*(42), 41148-41159,
836 doi:10.1074/jbc.M305837200.

837 Rudnick, R. L., and S. Gao (2014), Composition of the Continental Crust, 1-51, doi:10.1016/b978-0-
838 08-095975-7.00301-6.

839 Saito, M. A., and T. J. Goepfert (2008), Zinc–cobalt colimitation of Phaeocystis antarctica, *Limnol.*
840 *Oceanogr*, *53*(1), 266-275.

841 Saito, M. A., T. J. Goepfert, A. E. Noble, E. M. Bertrand, P. N. Sedwick, and G. R. DiTullio (2010), A
842 seasonal study of dissolved cobalt in the Ross Sea, Antarctica: micronutrient behavior, absence of
843 scavenging, and relationships with Zn, Cd, and P, *Biogeosciences*, *7*(12), 4059-4082, doi:10.5194/bg-
844 7-4059-2010.

845 Saito, M. A., T. J. Goepfert, and J. T. Ritt (2008), Some thoughts on the concept of colimitation: Three
846 definitions and the importance of bioavailability, *Limnol. Oceanogr*, *53*(1), 276-290.

847 Saito, M. A., and J. W. Moffett (2001), Complexation of cobalt by natural organic ligands in the
848 Sargasso Sea as determined by a new high-sensitivity electrochemical cobalt speciation method
849 suitable for open ocean work, *Marine chemistry*, *75*(1), 49-68.

850 Saito, M. A., and J. W. Moffett (2002), Temporal and spatial variability of cobalt in the Atlantic Ocean,
851 *Geochimica et Cosmochimica Acta*, *66*(11), 1943-1953, doi:10.1016/s0016-7037(02)00829-3.

852 Saito, M. A., J. W. Moffett, S. W. Chisholm, and J. B. Waterbury (2002), Cobalt limitation and uptake in
853 Prochlorococcus, *Limnology and Oceanography*, *47*(6), 1629-1636, doi:10.4319/lo.2002.47.6.1629.

854 Saito, M. A., J. W. Moffett, and G. R. DiTullio (2004), Cobalt and nickel in the Peru upwelling region: A
855 major flux of labile cobalt utilized as a micronutrient, *Global Biogeochemical Cycles*, *18*(4), n/a-n/a,
856 doi:10.1029/2003gb002216.

857 Saito, M. A., et al. (2016), The Acceleration of Dissolved Cobalt's Ecological Stoichiometry due to
858 Biological Uptake, Remineralization, and Scavenging in the Atlantic Ocean, *Biogeosciences*
859 *Discussions*, 1-43, doi:10.5194/bg-2016-511.

860 Saito, M. A., A. E. Noble, A. Tagliabue, T. J. Goepfert, C. H. Lamborg, and W. J. Jenkins (2013),
861 Slow-spreading submarine ridges in the South Atlantic as a significant oceanic iron source, *Nature*
862 *Geoscience*, *6*(9), 775-779, doi:10.1038/Ngeo1893.

863 Saito, M. A., G. Rocap, and J. W. Moffett (2005), Production of cobalt binding ligands in a
864 Synechococcus feature at the Costa Rica upwelling dome, *Limnology and Oceanography*, *50*(1), 279-
865 290, doi:10.4319/lo.2005.50.1.0279.

866 Saito, M. A., D. M. Sigman, and F. M. M. Morel (2003), The bioinorganic chemistry of the ancient
867 ocean: the co-evolution of cyanobacterial metal requirements and biogeochemical cycles at the
868 Archean–Proterozoic boundary?, *Inorganica Chimica Acta*, *356*, 308-318, doi:10.1016/S0020-
869 1693(03)00442-0.

870 Sañudo-Wilhelmy, S. A., C. J. Gobler, M. Okbamichael, and G. T. Taylor (2006), Regulation of
871 phytoplankton dynamics by vitamin B12, *Geophysical Research Letters*, *33*(4),
872 doi:10.1029/2005gl025046.

873 Shaked, Y., Y. Xu, K. Leblanc, and F. M. M. Morel (2006), Zinc availability and alkaline phosphatase
874 activity in Emiliania huxleyi: Implications for Zn-P co-limitation in the ocean, *Limnology and*
875 *Oceanography*, *51*(1), 299-309, doi:10.4319/lo.2006.51.1.0299.

876 Shelley, R. U., et al. (2012), Controls on dissolved cobalt in surface waters of the Sargasso Sea:
877 Comparisons with iron and aluminum, *Global Biogeochemical Cycles*, *26*, doi:Artn Gb2020
878 10.1029/2011gb004155.

879 Shelley, R. U., N. J. Wyatt, G. A. Tarran, A. P. Rees, P. J. Worsfold, and M. C. Lohan (2016), A tale of
880 two gyres: Contrasting distributions of dissolved cobalt and iron in the Atlantic Ocean during an
881 Atlantic Meridional Transect (AMT-19), *Progress in Oceanography*, doi:10.1016/j.pocean.2016.10.013.

882 Sunda, W. G., and S. A. Huntsman (1988), Effect of Sunlight on Redox Cycles of Manganese in the
883 Southwestern Sargasso Sea, *Deep-Sea Res*, *35*(8), 1297-1317, doi:Doi 10.1016/0198-
884 0149(88)90084-2.

885 Sunda, W. G., and S. A. Huntsman (1995), Cobalt and zinc interreplacement in marine phytoplankton:
886 Biological and geochemical implications, *Limnology and Oceanography*, *40*, 1404-1417.

887 Sundby, B., L. G. Anderson, P. O. Hall, Å. Iverfeldt, M. M. R. van der Loeff, and S. F. Westerlund
888 (1986), The effect of oxygen on release and uptake of cobalt, manganese, iron and phosphate at the
889 sediment-water interface, *Geochimica et Cosmochimica Acta*, *50*(6), 1281-1288.

890 Swanner, E. D., N. J. Planavsky, S. V. Lalonde, L. J. Robbins, A. Bekker, O. J. Rouxel, M. A. Saito, A.
891 Kappler, S. p. J. Mojzsis, and K. O. Konhauser (2014), Cobalt and marine redox evolution, *Earth and
892 Planetary Science Letters*, *390*, 253-263, doi:10.1016/j.epsl.2014.01.001.

893 Tagliabue, A., et al. (2016), How well do global ocean biogeochemistry models simulate dissolved iron
894 distributions?, *Global Biogeochemical Cycles*, doi:10.1002/2015gb005289.

895 Tagliabue, A., and J. A. Resing (2016), Impact of hydrothermalism on the ocean iron cycle,
896 *Philosophical Transactions of the Royal Society A: Mathematical, Physical and Engineering Sciences*,
897 *374*(2081), 20150291, doi:10.1098/rsta.2015.0291.

898 Twining, B. S., and S. B. Baines (2013), The trace metal composition of marine phytoplankton, *Annual
899 review of marine science*, *5*, 191-215, doi:10.1146/annurev-marine-121211-172322.

900 Twining, B. S., S. B. Baines, J. B. Bozard, S. Vogt, E. A. Walker, and D. M. Nelson (2011), Metal
901 quotas of plankton in the equatorial Pacific Ocean, *Deep-Sea Res Pt Ii*, *58*(3-4), 325-341,
902 doi:10.1016/j.dsr2.2010.08.018.

903 Twining, B. S., S. Rauschenberg, P. L. Morton, and S. Vogt (2015), Metal contents of phytoplankton
904 and labile particulate material in the North Atlantic Ocean, *Progress in Oceanography*, *137*, 261-283,
905 doi:10.1016/j.pocean.2015.07.001.

906 Wojciechowski, C. L., J. P. Cardia, and E. R. Kantrowitz (2002), Alkaline phosphatase from the
907 hyperthermophilic bacterium T. maritima requires cobalt for activity, *Protein Sci*, *11*(4), 903-911,
908 doi:10.1110/ps.4260102.

909 Xu, Y., D. Tang, Y. Shaked, and F. M. Morel (2007), Zinc, cadmium, and cobalt interreplacement and
910 relative use efficiencies in the coccolithophore Emiliania huxleyi, *Limnology and Oceanography*, *52*(5),
911 2294-2305.

912 Zhang, H., C. M. Van Den Berg, and R. Wollast (1990), The determination of interactions of cobalt (II)
913 with organic compounds in seawater using cathodic stripping voltammetry, *Marine Chemistry*, *28*(4),
914 285-300.
915
916

Figure Legends
918
919 **Figure 1.** Global cobalt data vertical distribution. Bars represent the standard deviation around the
920 mean cobalt (pM) from each vertical bin (see methods). The blue line represents the model mean
921 vertical profile extracted at the same location as the data while the red line represents the overall mean
922 vertical profile of the model.
923
924 **Figure 2.** Observed vs modelled dCo (annual mean, pM) for different depth slices
925
926 **Figure 3** Observed vs modelled dCo (annual mean, pM) for specific GEOTRACES and CLIVAR
927 sections
928
929 **Figure 4.** Observed vs modelled dCo (annual mean, pM) for two zonal Atlantic GEOTRACES sections
930 when modelled oxygen is restored to World Ocean Atlas 2009 values
931
932 **Figure 5.** Free cobalt (pM) and the proportion of dCo that is free (no units) at the surface and at 250m
933
934 **Figure 6.** Absolute change in dCo (pM) at the surface (0-50m) and at 250m for no dust (panel a), no
935 sediment supply (panels c and d), no sediment supply at low bottom water O_2 (panels f and g) and the
936 percentage of the total change due to sediment supply caused by low bottom water O_2 sediment supply
937 (panels I and j). Panels b, e and h shows the annually averaged surface dCo from the no dust, no
938 sediment and no sediment supply at low bottom water O_2 – please compare to Fig 2a.
939
940 **Figure 7.** Absolute change in dCo (pM) at the surface and 250m, when Co scavenging is not reduced at
941 low oxygen levels (panels a and b) and not reduced by low rates of bacterial activity (panels c and d)
942
943 **Figure 8.** How different processes shape the Co plume observed on GP-16. Top row shows model and
944 data dCo (pM, panels a and b, respectively), while middle and bottom rows show the proportional
945 change in dCo when there is no sediment supply (panel c), no enhanced sediment flux at low O_2 (panel
946 d), no reduction in scavenging at low O_2 (panel e) and no reduction in scavenging at low rates of
947 bacterial activity (panel f). Thick and thin contours highlight where a given process affects 50 and 25%
948 of the magnitude of the dCo plume, respectively.
949
950 **Figure 9.** Total fluxes of dCo linked to various external sources (panels a and b) and internal cycling
951 (panels c-f). All fluxes are depth integrated and are presented in units of μmol Co m^{-2} yr^{-1}.
952
953 **Figure 10.** The magnitude of different processes in the modelled global Cobalt budget (mol Co yr-1).
954
955 **Figure 11.** Zonal mean dissolved Cobalt (pM) from the Atlantic and Pacific oceans. Zonal mean PO$_4$
956 (μM) is overlain as a contour.
957
958 **Figure 12.** Annual mean Co/P quotas in nanophytoplankton and diatoms at 0-50m (panels a and b).
959 Annual minimum Co/P quotas in nanophytoplankton and diatoms at 0-50m using monthly model
960 output (panels c and d). Annual mean Co/P ratios in all particles for 0-50 and 1000-1500m (panels e
961 and f). All are in units of μmol Co / mol P.
962
963 **Figure 13.** A map of the degree to which cobalt uptake is enhanced by Zn availability as per Eqn 6
964 (unitless).

1.

2.
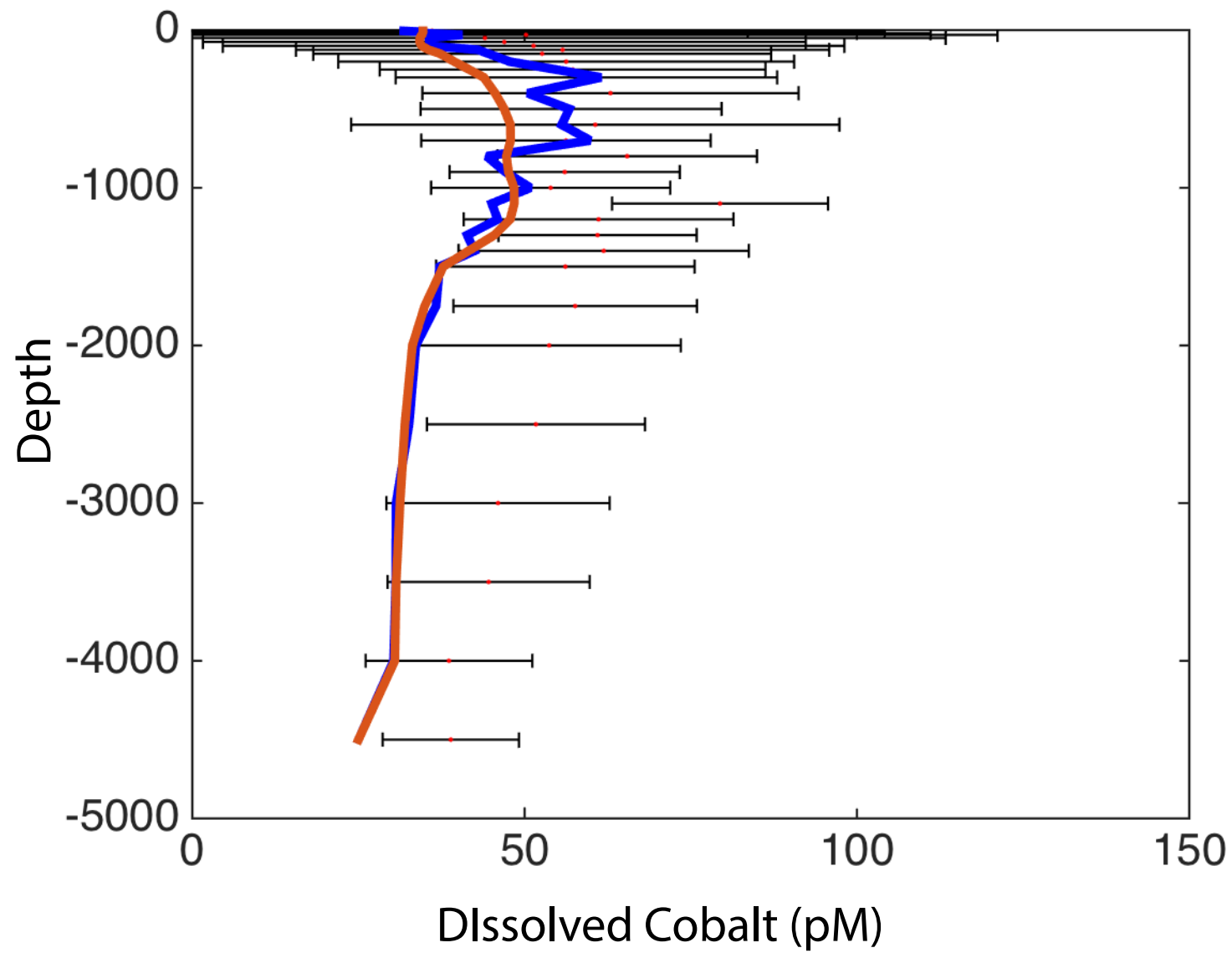
a) 0-50m
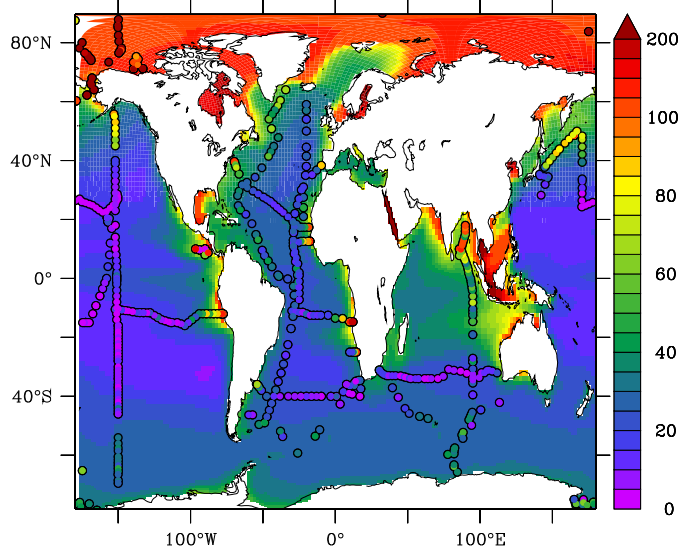
b) 100-200m
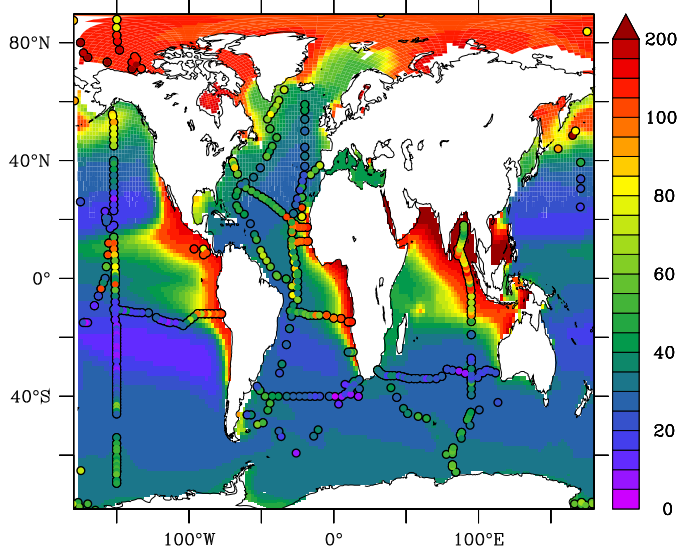
c) 400-500m
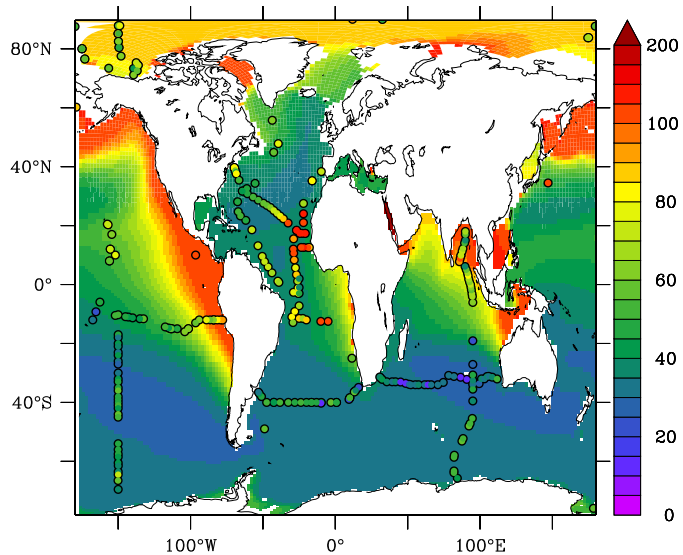
d) 700-800m
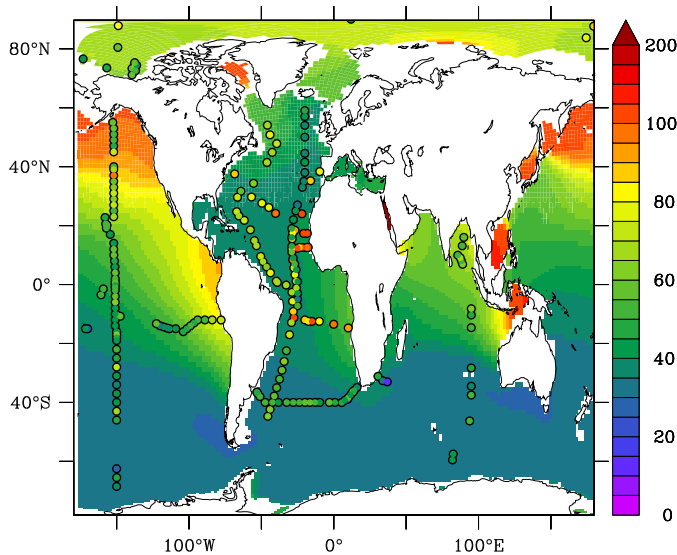
e) 900-1000m

f) 2500-3000m

3.
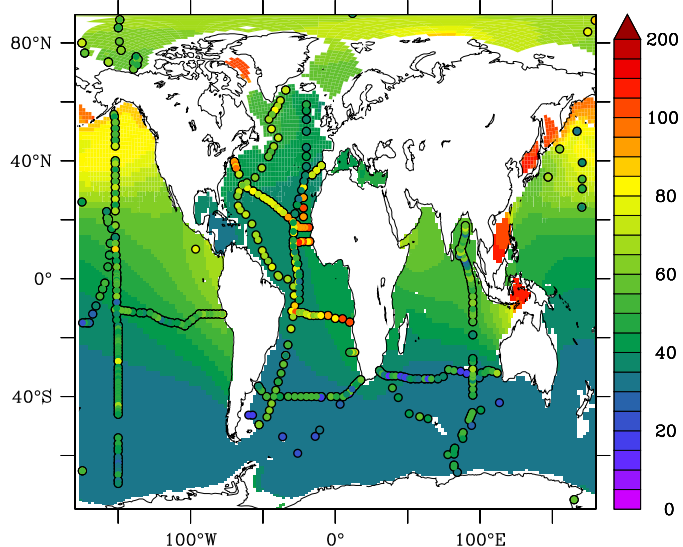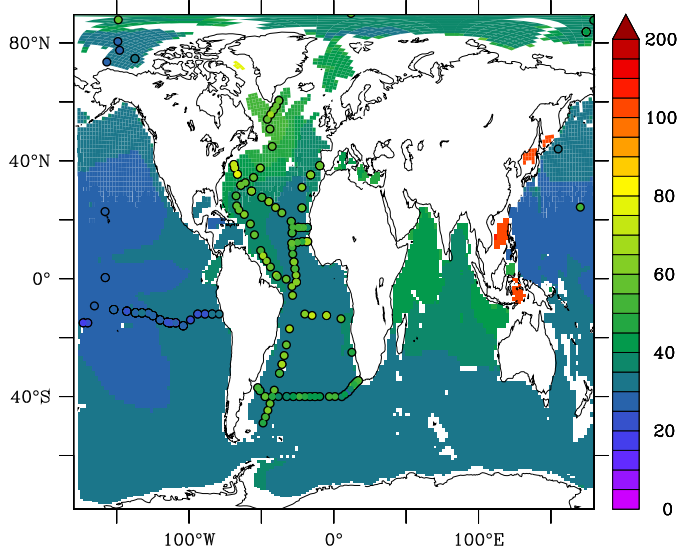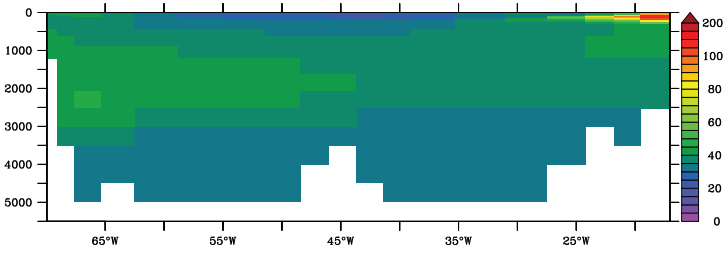
a) GA-03

Cruise Track
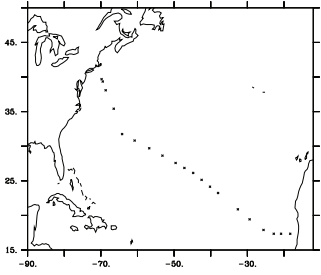
Observations
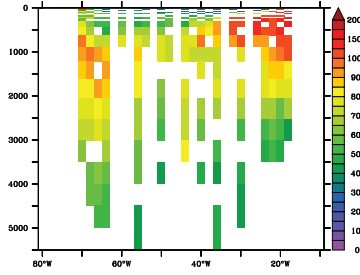
b) CoFeMUG
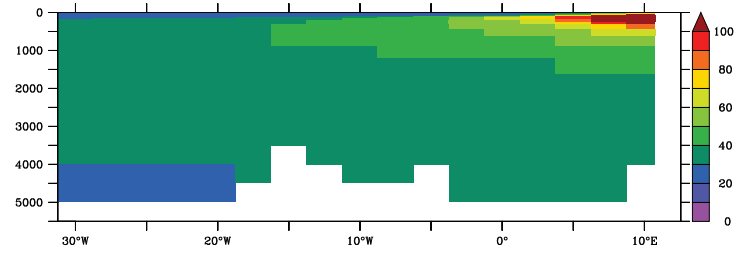
Cruise Track
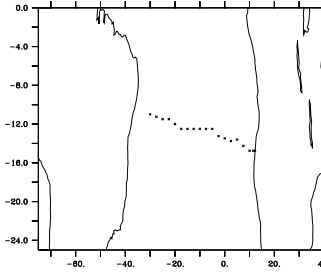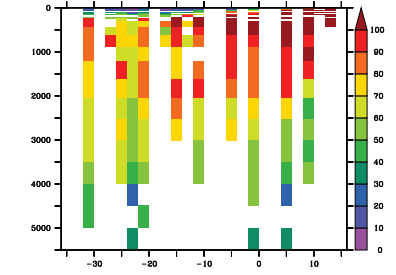
Observations

c) GP-16
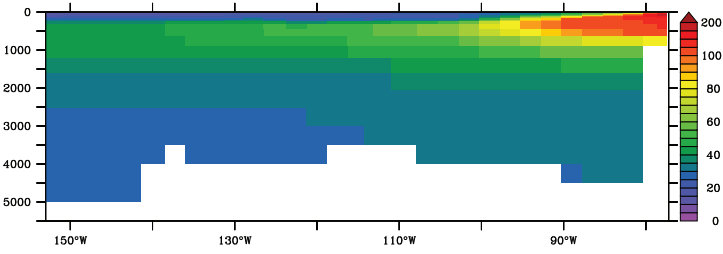
Cruise Track
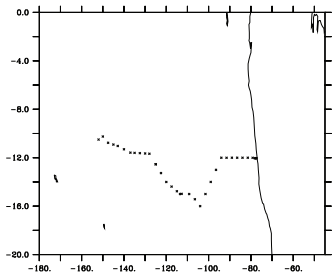
Observations
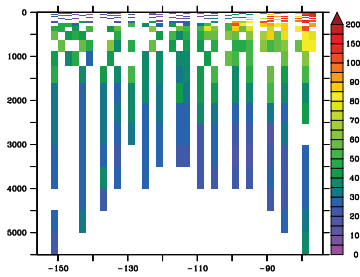
d) I8/I9

Cruise Track

Observations

4.

a) GA-03

b) CoFeMUG

Cruise Track

Observations

Cruise Track

Observations

5.
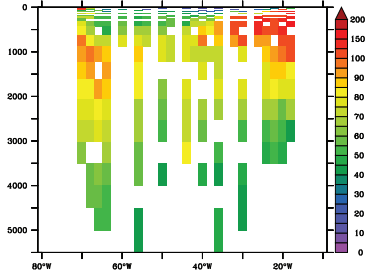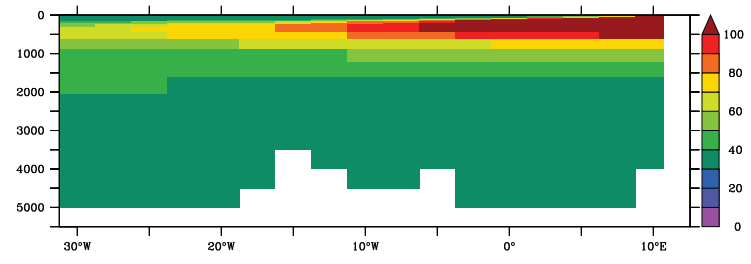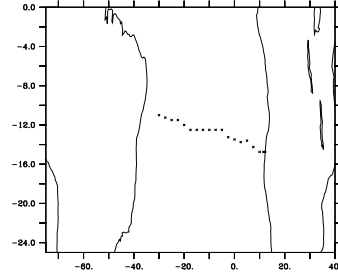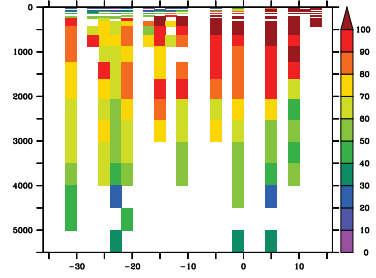
a) Cobalt Prime (surface, pM)
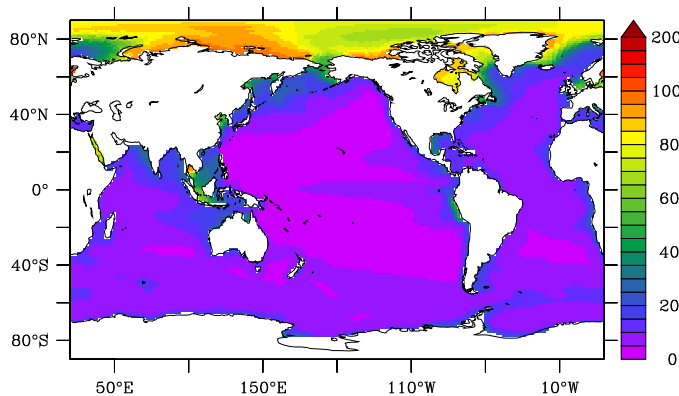
b) Cobalt Prime / Dissolved Cobalt (surface, no units)
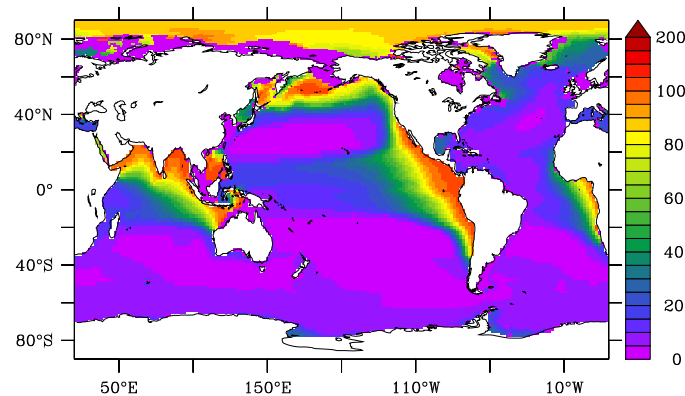
c) Cobalt Prime (250m, pM)
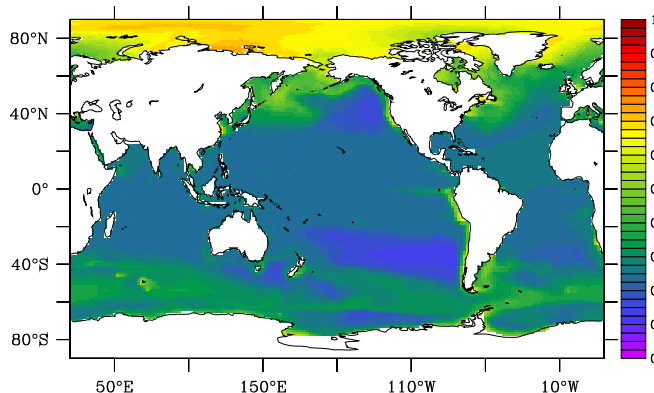
d) Cobalt Prime / Dissolved Cobalt (250m, no units)

6.
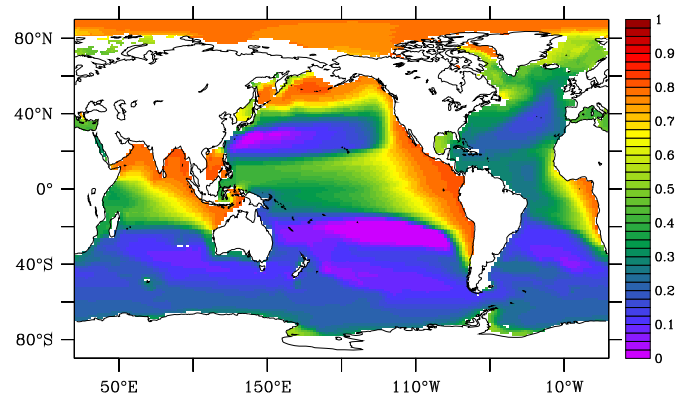
a) ΔdCo, no dust (surf, pM)
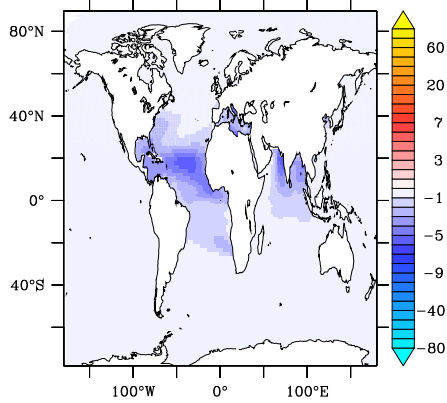
b) dCo, no dust (surf, pM)
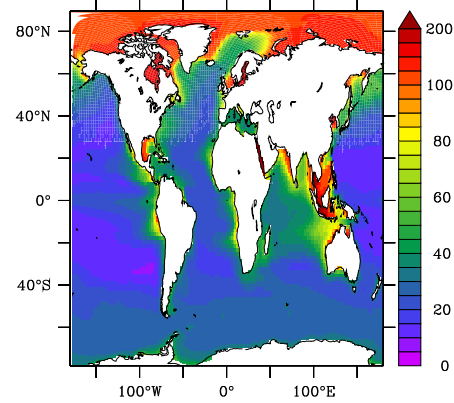
c) ΔdCo, no sediment (surf, pM)
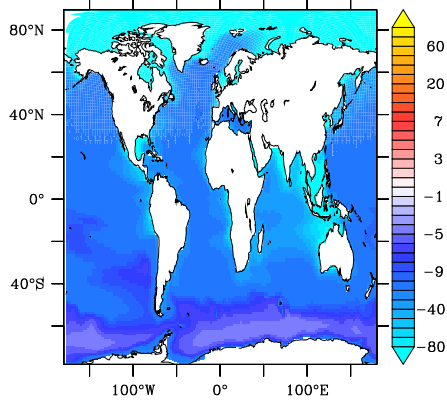
d) ΔdCo, no sediment (250m, pM)
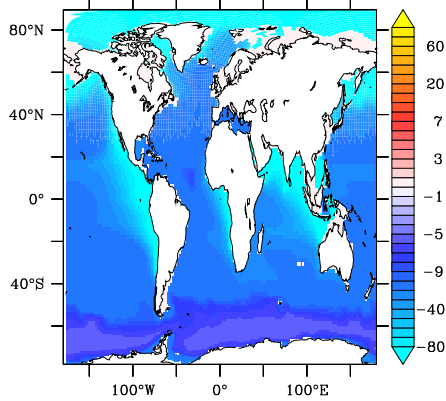
e) dCo, no sediment (surf, pM)
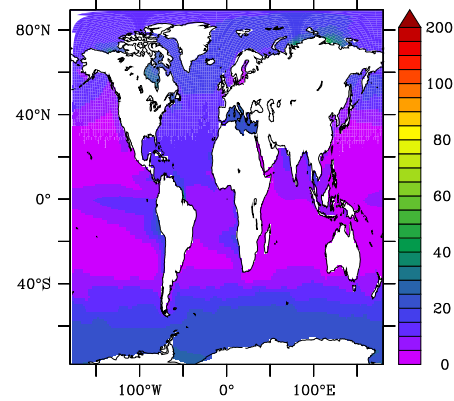
f) ΔdCo, no low O₂ sed (surf, pM)
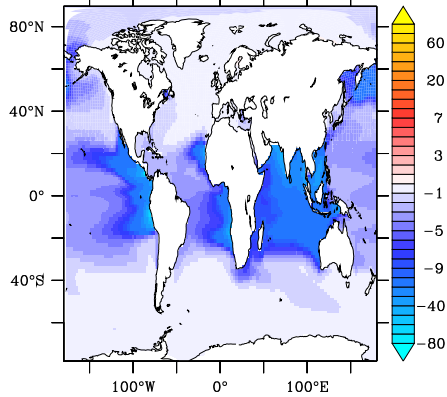
g) ΔdCo, no low O₂ sed (250m, pM)
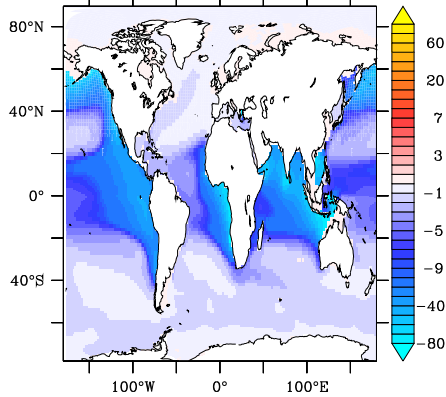
h) dCo, no low O₂ sed (surf, pM)
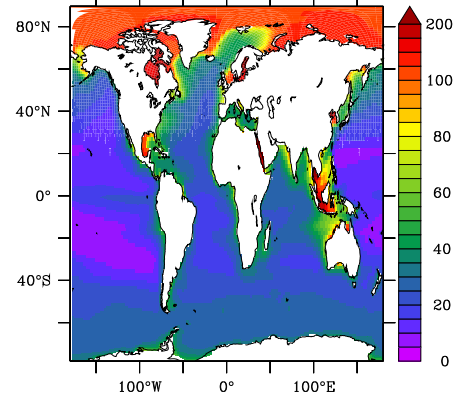
i) Impact of no low O₂ sed on dCo (surf, %)
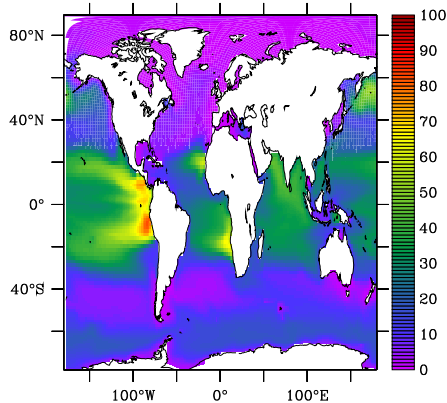
j) Impact of no low O₂ sed on dCo (250m, %)

7.
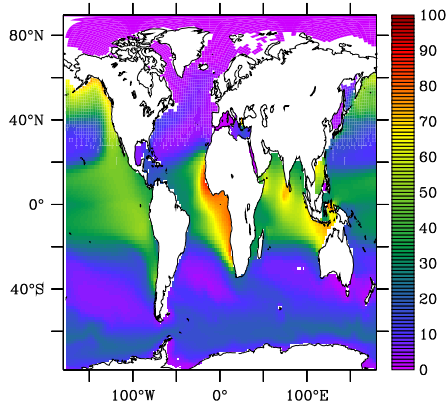
a) ΔdCo, O$_2$ does not affect scavenging (surf, pM)
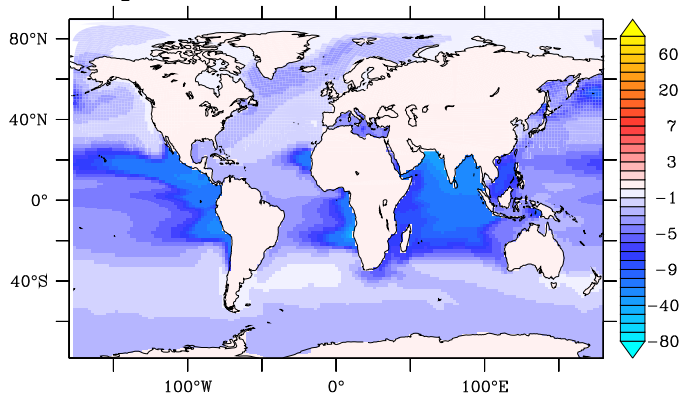
b) ΔdCo, O$_2$ does not affect scavenging (250m, pM)
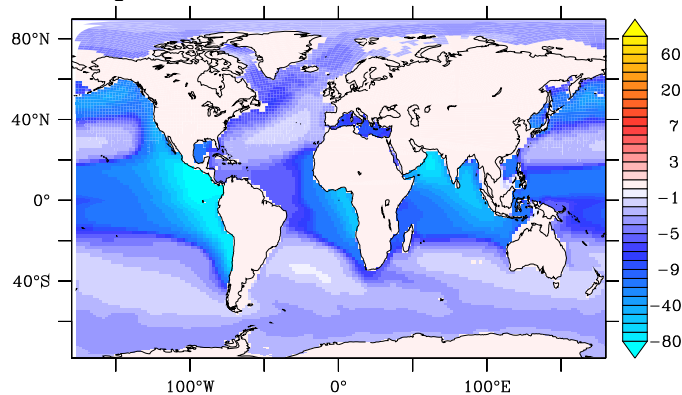
c) ΔdCo, Bact does not affect scavenging (surf, pM)

d) ΔdCo, Bact does not affect scavenging (250m, pM)

8.
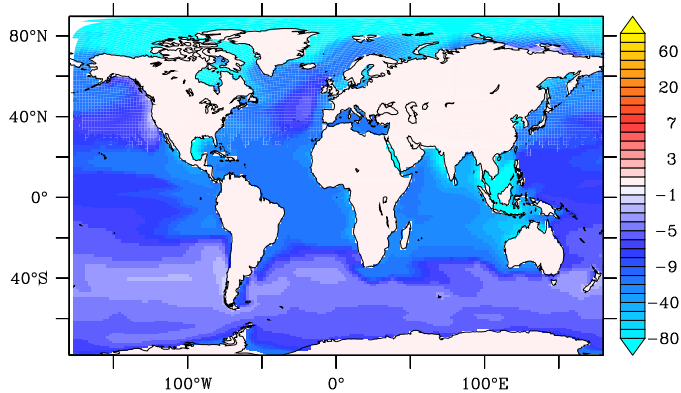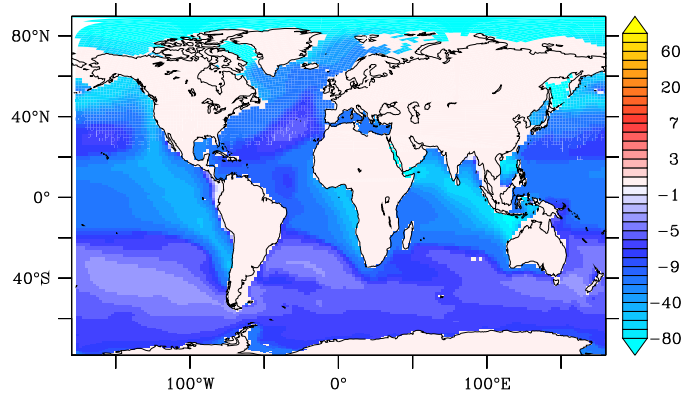
a) Modelled dCo (GP-16, pM)
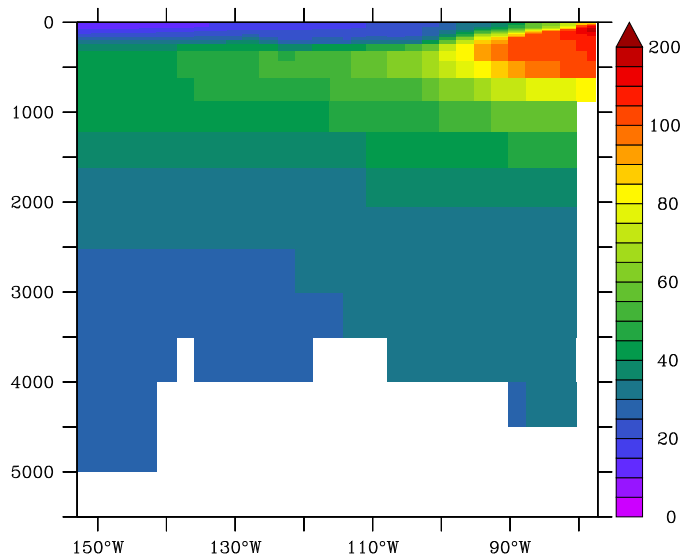
b) Observed dCo (GP-16, pM)
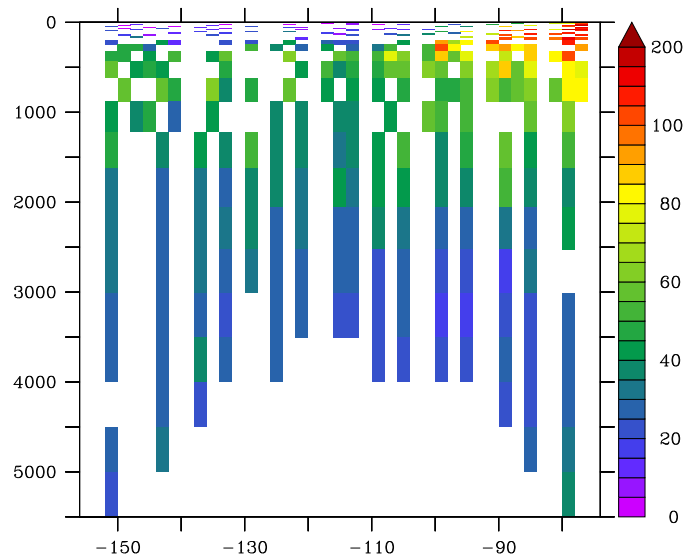
c) ΔdCo/dCo, no sediment (GP-16, no units)
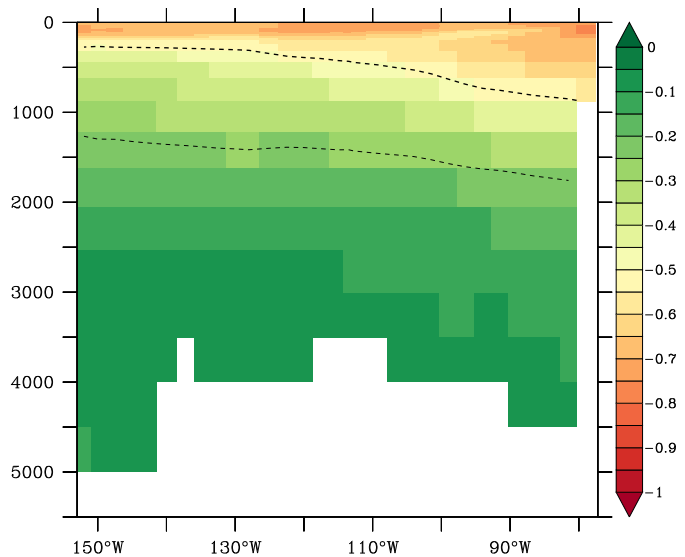
d) ΔdCo/dCo, no low O_2 sed (GP-16, no units)
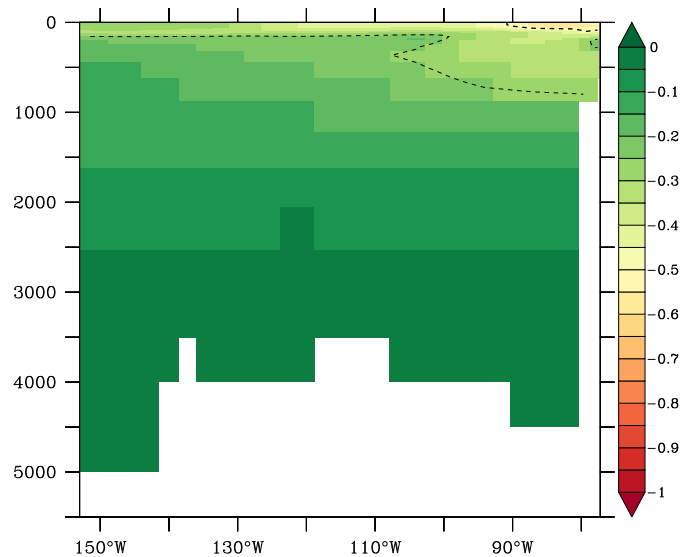
e) ΔdCo/dCo, no O_2 scav (GP-16, no units)
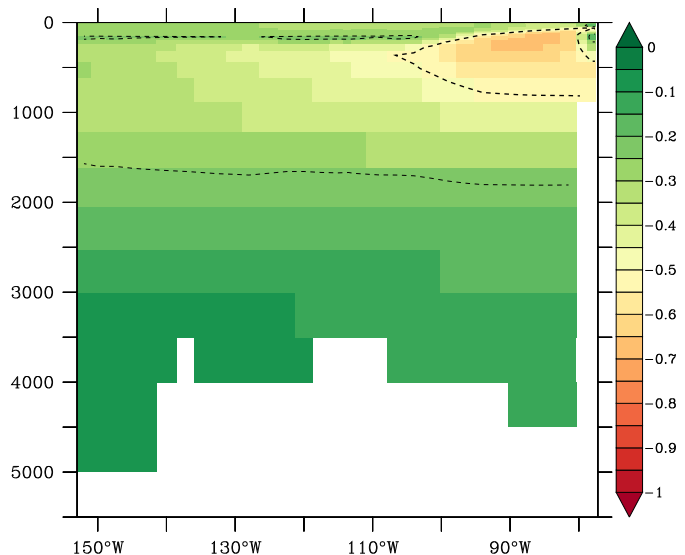
f) ΔdCo/dCo, no Bact scav (GP-16, no units)

9.
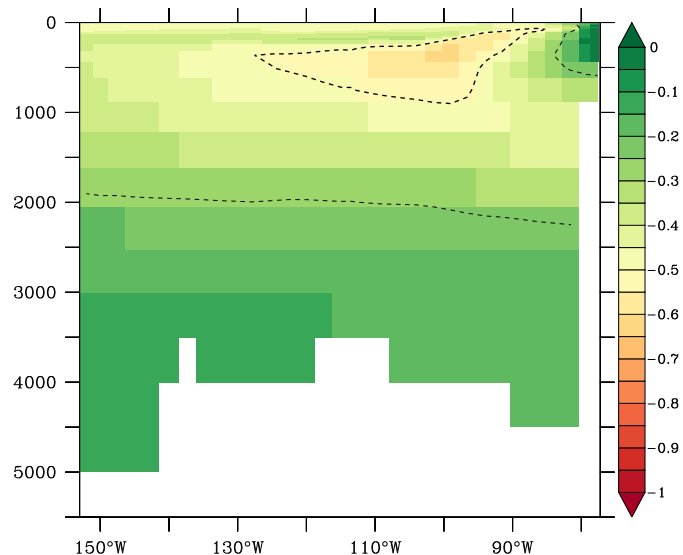
a) dCo supply from dust
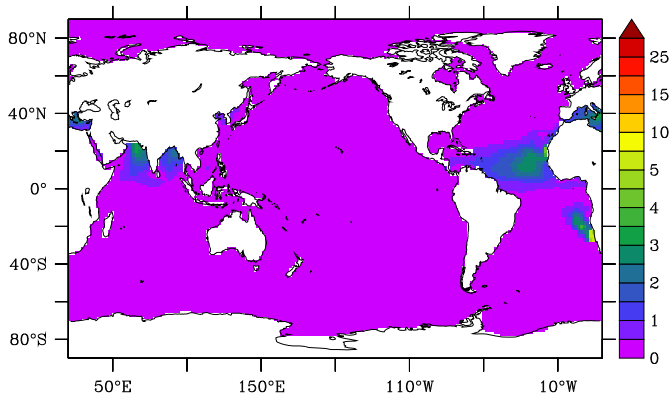
b) dCo supply from sediments
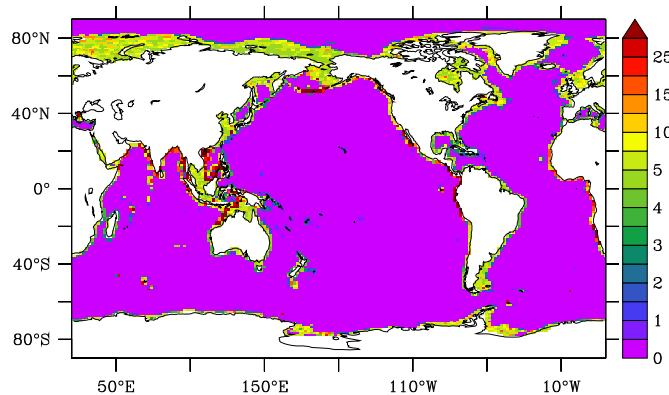
c) dCo consumption by biological uptake
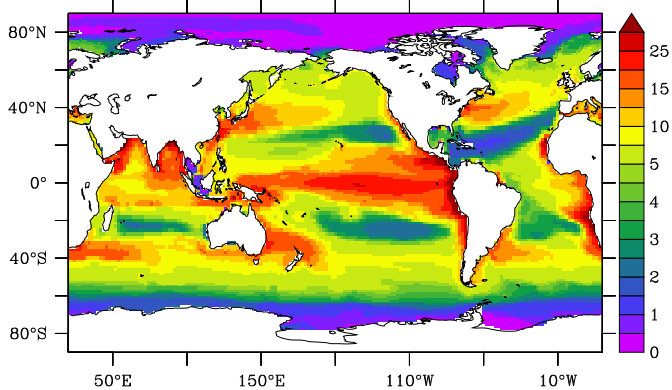
d) dCo supply from pCo regeneration
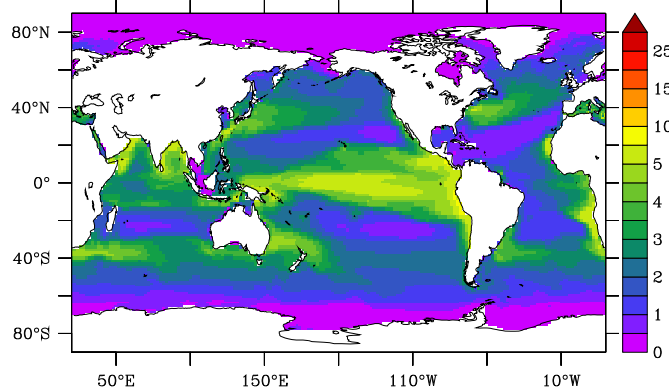
e) dCo consumption by scavenging
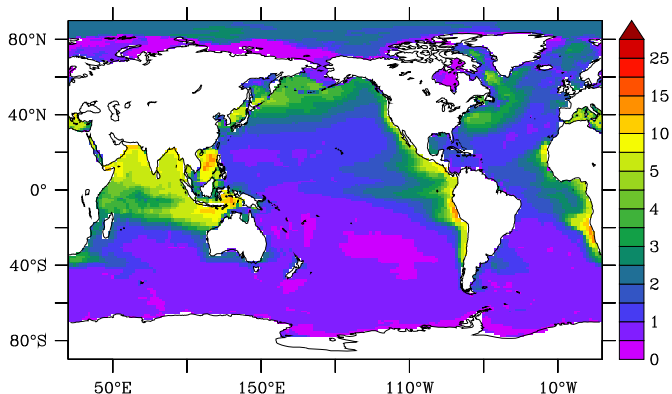
f) dCo supply from scCo dissolution

10.

11.
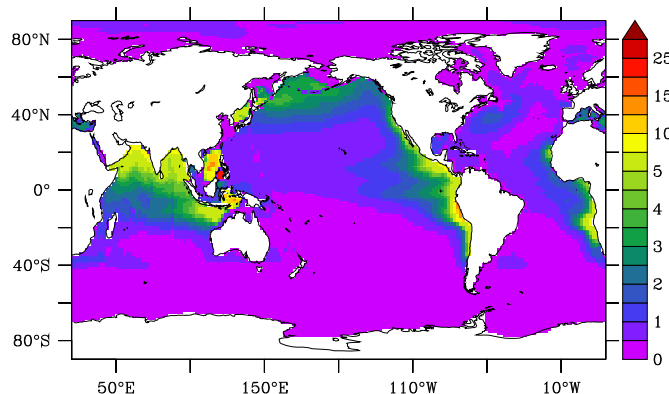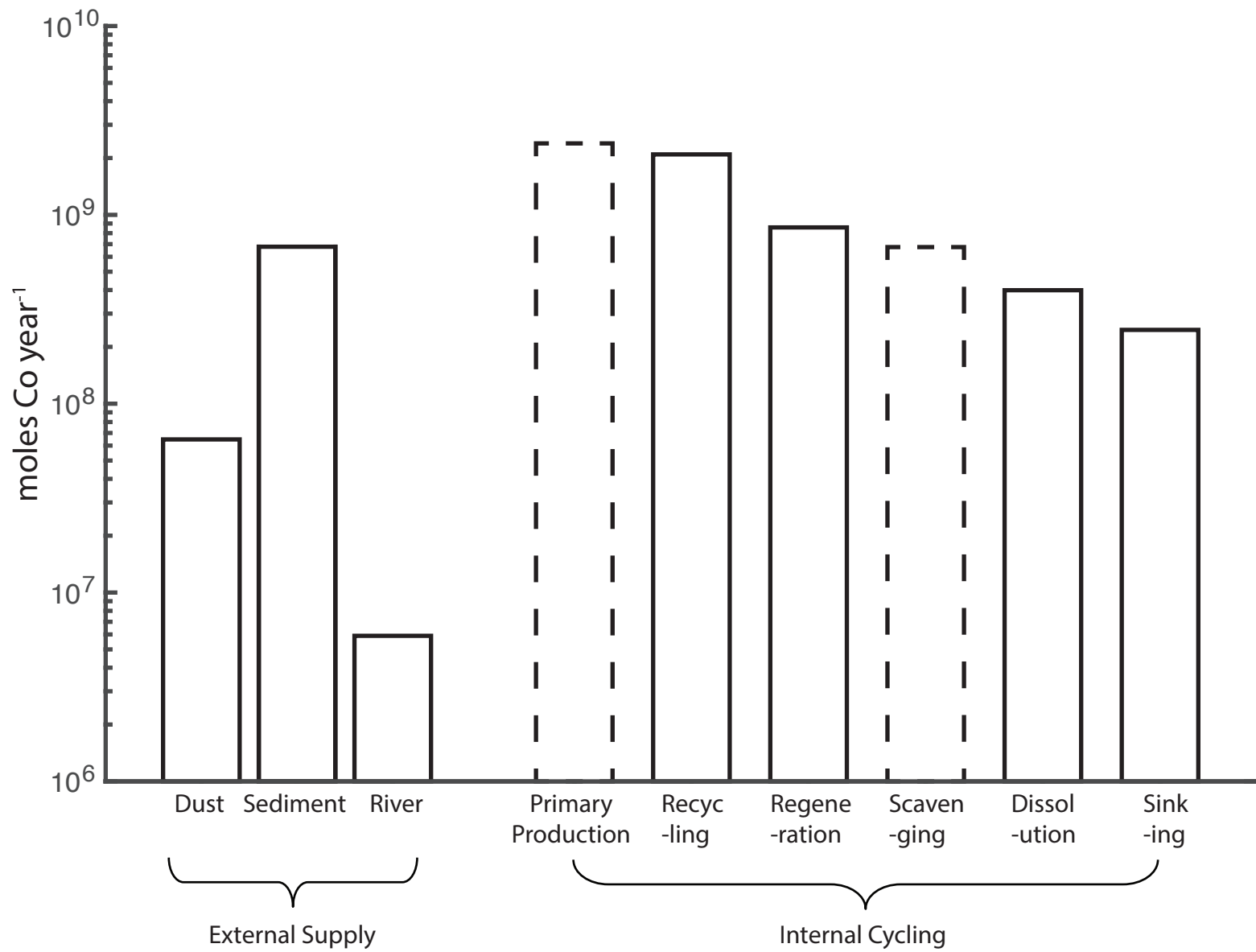
a) Atlantic Ocean zonal mean
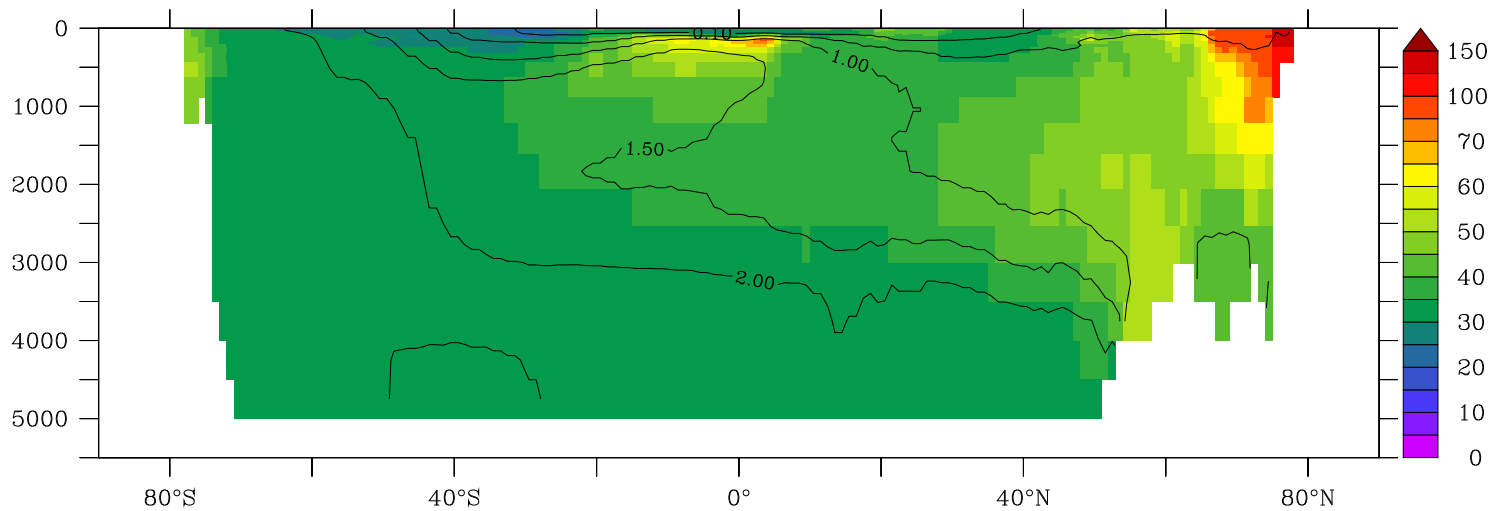
a) Pacific Ocean zonal mean

12.
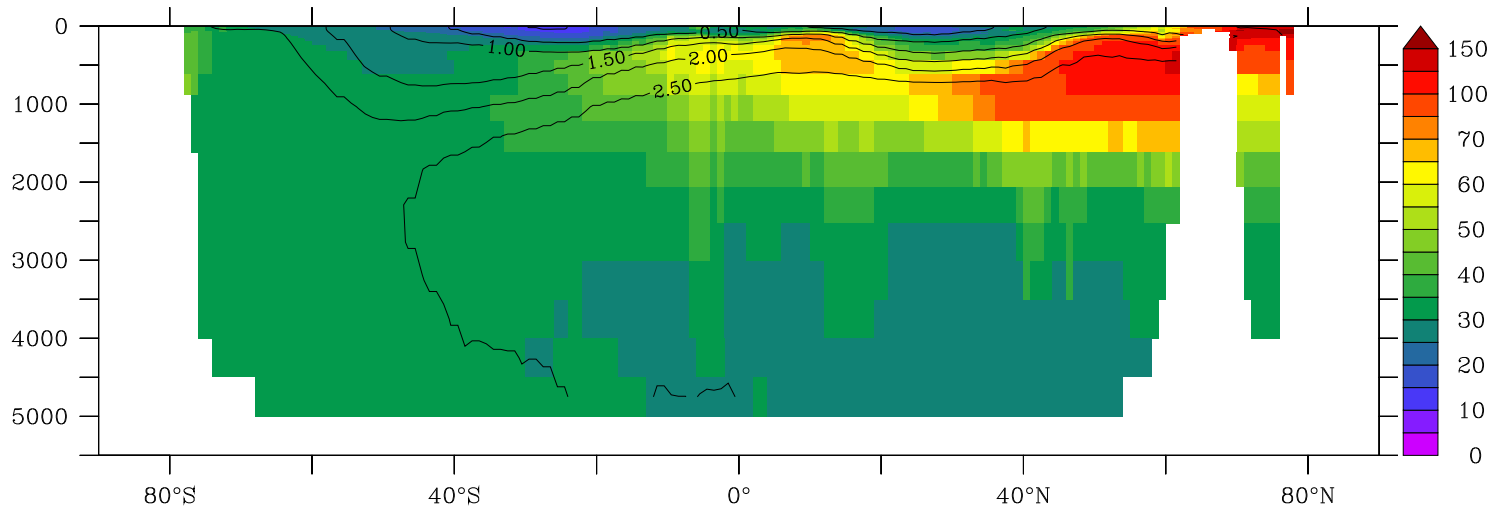
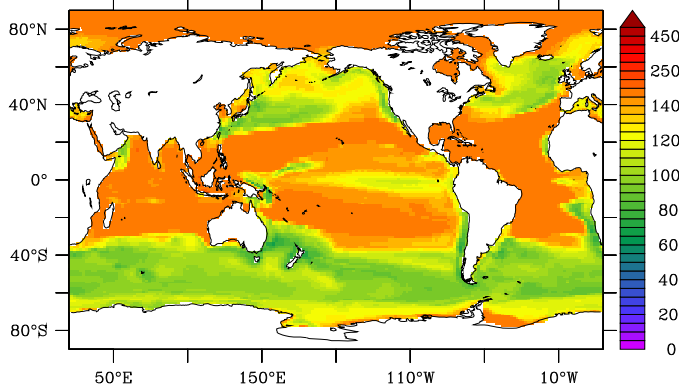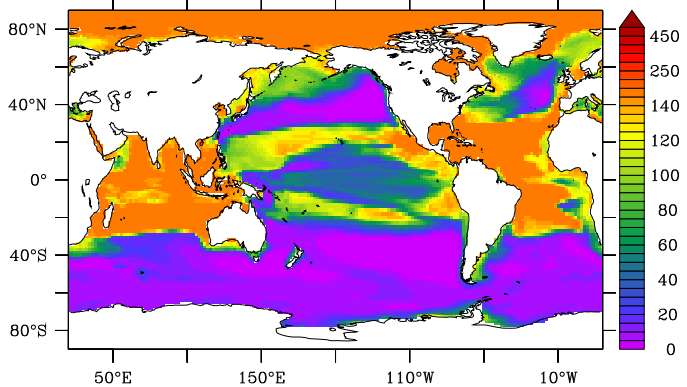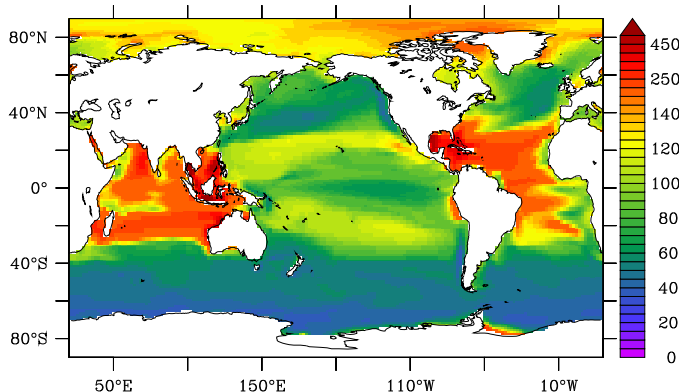a) Co/P, nanophyt. (µmol/mol, 0-50m)
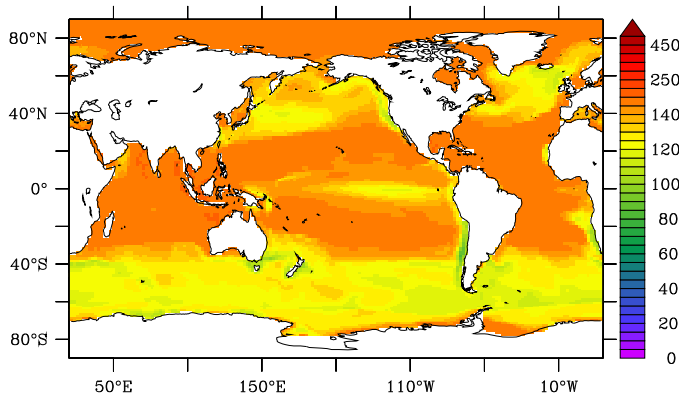
b) Co/P, diatoms. (µmol/mol, 0-50m)
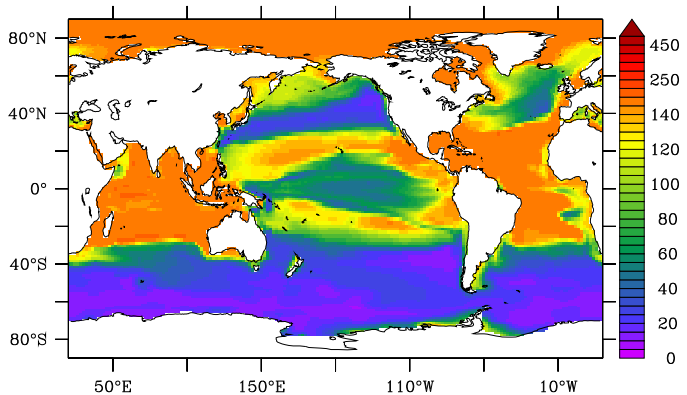
c) Co/P, nanophyt. (µmol/mol, 0-50m, annual min)

d) Co/P, diatoms. (µmol/mol, 0-50m, annual min)

e) Co/P, particles. (µmol/mol, 0-50m)
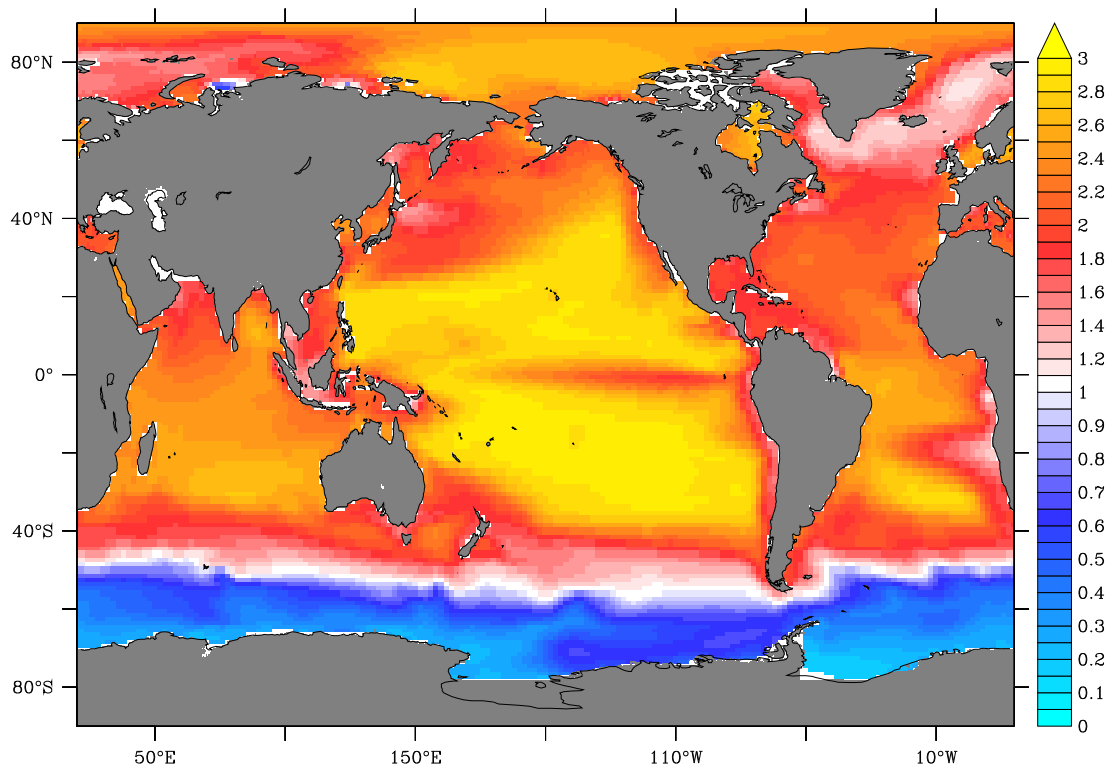
f) Co/P, particles. (µmol/mol, 1000-1500m)

13.
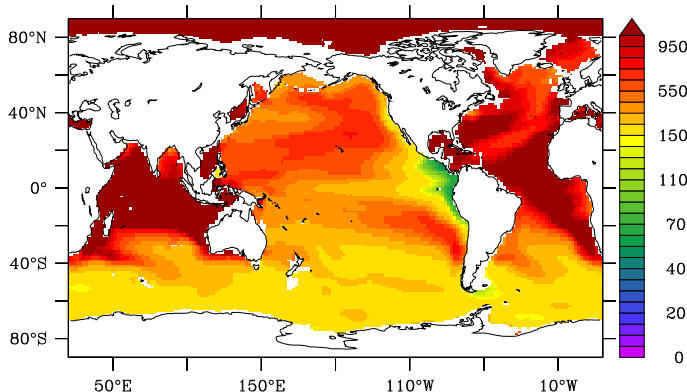
Relative impact of Zn availability on Co uptake

Table 1. Model parameter values. Where two values are given, the first is for nanophytoplankton and the second is for diatoms

Parameter	Value	Units	Description
O_{2thres_1}	50	$\mu M\ O_2$	Threshold for enhanced sedimentary Co fluxes
O_{2thres_2}	2	$\mu M\ O_2$	Threshold for eliminated sedimentary Co fluxes
θ_{MAX}	150 / 150	$\mu mol\ Co\ mol\ P^{-1}$	Maximum phytoplankton Co quotas
kdCo	50 / 80	pM Co	Half saturation constants for Co uptake
KZnCo	0.5	nM Zn	Half saturation constant for Zn – Co interaction for diatom group only
ΛCo_{MIN}	0.1×10^{-3}	d^{-1}	Minimum dCo scavenging rate
ΛCo	0.01	d^{-1}	Maximum dCo scavenging rate
O_{2ST}	100	$\mu M\ O_2$	Threshold for O_2 effect on scavenging
$kO_2\Lambda$	25	$\mu M\ O_2$	Half saturation constant for O_2 effect on scavenging and dissolution
$kB\Lambda$	2.5	$\mu M\ C$	Half saturation constant for Bacterial effect on scavenging
$kPAR\Lambda$	15	$W\ m^{-2}$	Half saturation constant for PAR effect on scavenging
O_{2DT}	50	$\mu M\ O_2$	Threshold for O_2 effect on sCo dissolution
λ_{MAX}	0.1	d^{-1}	Maximum sCo dissolution rate
CoL_{MIN}	25	pM	Minimum concentration of Co ligands
θ_{ZOO}	20	$\mu mol\ Co\ mol\ P^{-1}$	Zooplankton Co quota
ϕ	1.5	unitless	Relative rate of particulate organic Co remineralisation

Table 2. Major fluxes of the modelled Cobalt cycle.

External Inputs	Internal Cycling	Value
Dust		6.5×10^7 moles per year
Sediment		6.8×10^8 moles per year
River		5.7×10^6 moles per year
Total		7.5×10^8 moles per year
	Primary Production	24×10^8 moles per year
	Recycling	21×10^8 moles per year
	Regeneration	8.6×10^8 moles per year
	Scavenging	6.8×10^8 moles per year
	Dissolution	4.0×10^8 moles per year
	Sinking PCo (250m)	2.5×10^8 moles per year

Global dCo Inventory	5×10^{10} moles
Residence Time (Global)	250 years
Residence Time (0-250m)	7 Years